Mapping upper mantle discontinuities beneath the Australian continent using multimode surface waves and receiver functions

K. Tarumi[1,*] and K. Yoshizawa[1,2]

[1] Department of Natural History Sciences, Graduate School of Science, Hokkaido University, Sapporo 060-0810, Japan

[2]Department of Earth & Planetary Sciences, Faculty of Science, Hokkaido University, Sapporo 060-0810, Japan.

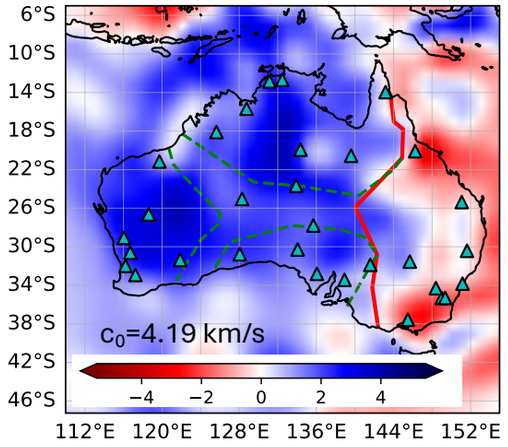
[*]Corresponding author: tarumi.kotaro.jp@gmail.com

This is a preprint that is submitted to EarthArXiv. The original manuscript has been submitted to Physics of the Earth and Planetary Interiors.

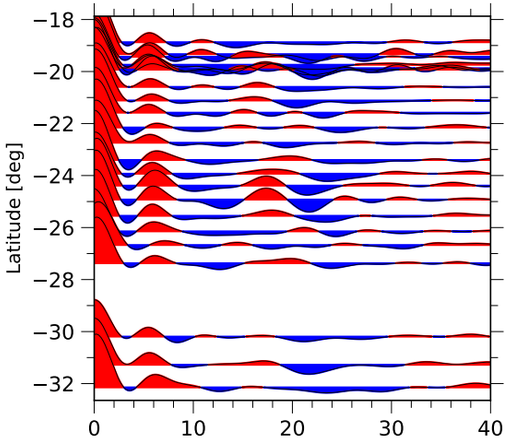
Graphical Abstract

Surface-wave dispersion data & Receiver Functions

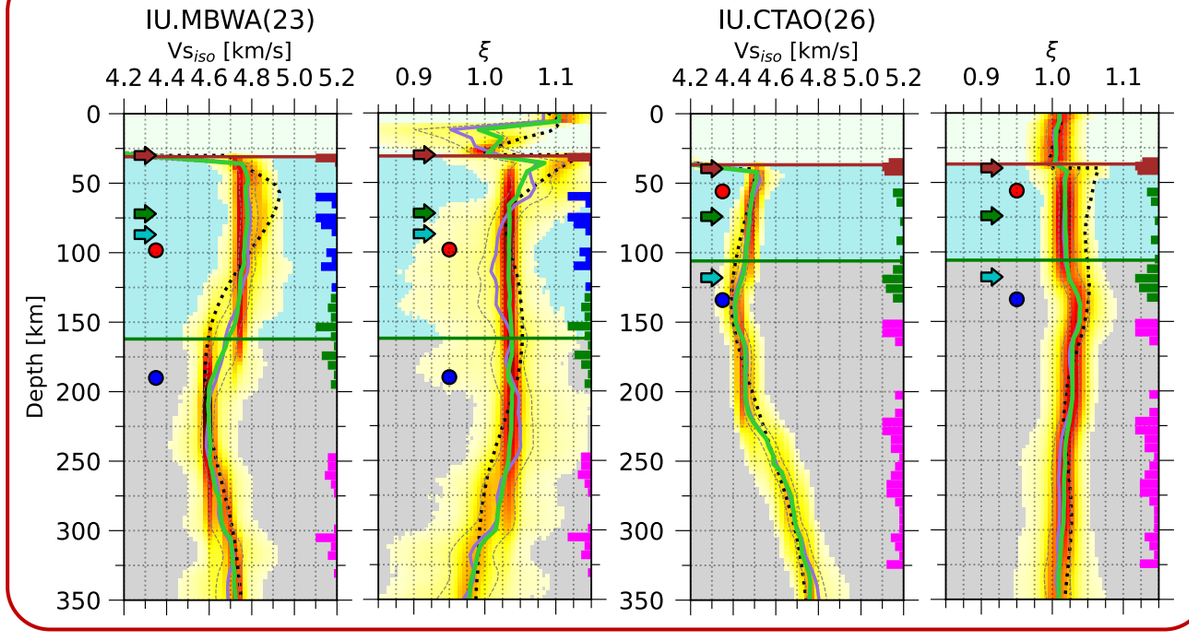
Phase speed perturbation of fundamental Rayleigh (125.0 s)



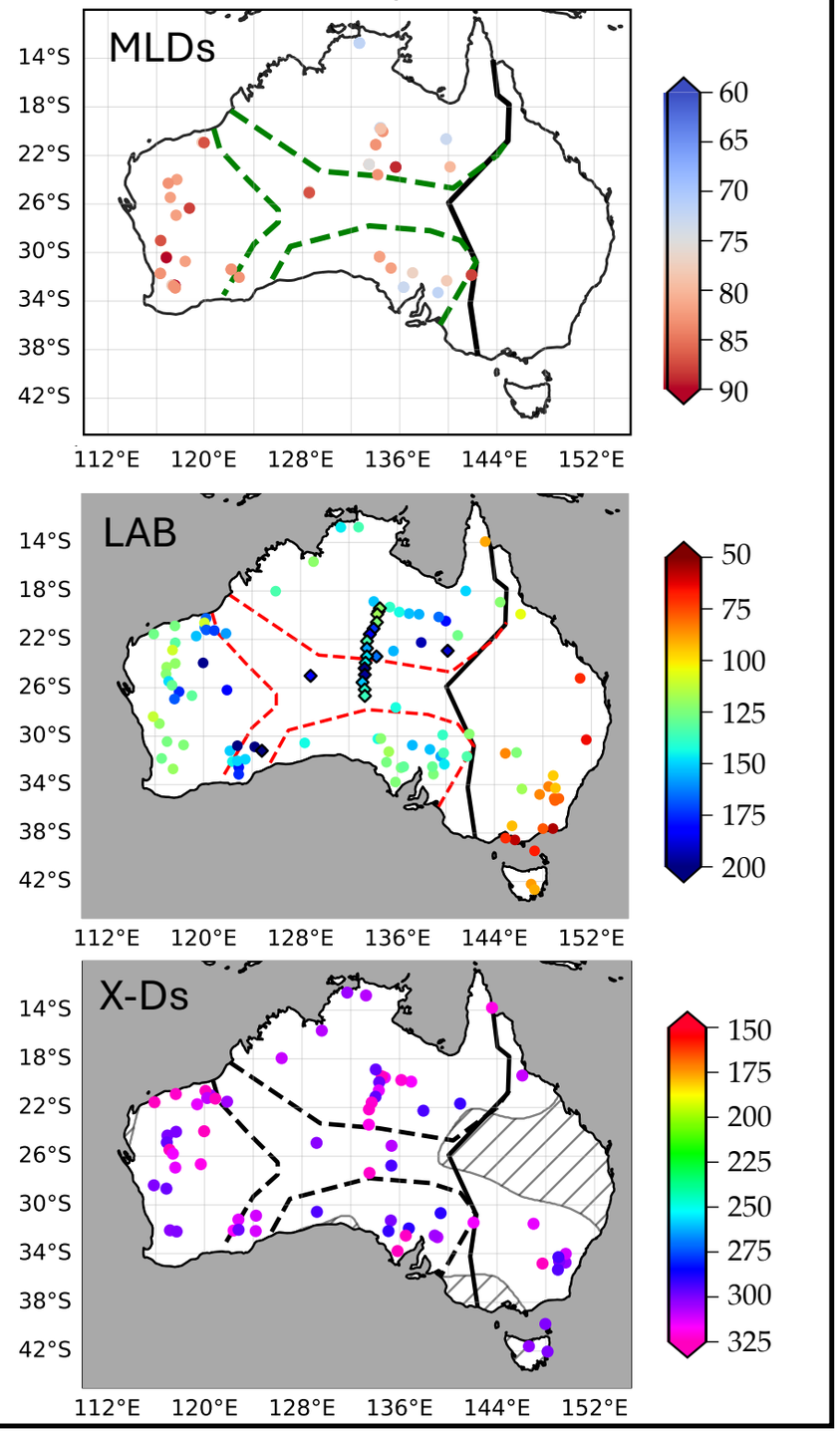
P-wave Receiver Functions obtained at BILBY



Joint Bayesian analyses & Discontinuity Detection



Discontinuity mapping



Manuscript File Click here to view linked References

Highlights

Mapping upper mantle discontinuities beneath the Australian continent using multimode surface waves and receiver functions

Kotaro Tarumi,Kazunori Yoshizawa

- Upper mantle discontinuity maps beneath the Australian continent are constructed.
- Multimode surface waves and receiver functions are used to constrain discontinuities.
- LAB is shallow in the eastern Phanerozoic area and deepens westward under cratons.
- Multiple MLDs in cratonic areas show either positive or negative velocity changes.
- Multiple X-discontinuities beneath LAB accompany the weakening of radial anisotropy.

Mapping upper mantle discontinuities beneath the Australian continent using multimode surface waves and receiver functions

Kotaro Tarumi[a,b,*], Kazunori Yoshizawa[a,b]

[a]Department of Natural History Sciences, Graduate School of Science, Hokkaido University, Sapporo, 060-0810, Japan
[b]Department of Earth and Planetary Sciences, Faculty of Science, Hokkaido University, Sapporo, 060-0810, Japan

ARTICLE INFO

Keywords:
Australia
Lithosphere
Asthenosphere
Mid-Lithospheric Discontinuity
X-Discontinuity
Receiver function
Surface waves

ABSTRACT

Spatial distributions of upper mantle discontinuities beneath the Australian continent are mapped using a large number of station-based 1-D S-velocity profiles with radial anisotropy, derived from joint Bayesian inversions of multimode surface waves and P-wave receiver functions. Numerous permanent and temporary stations across Australia enable us to constrain localized seismic velocity structures, including the lithospheric-asthenosphere boundary (LAB), mid-lithospheric discontinuities (MLDs), and X-discontinuities (X-Ds) below the LAB, providing quantitative constraints on the variations of seismic velocity and radial anisotropy across these interfaces. Subsequent statistical cluster analysis of locally detected discontinuities identifies multiple MLDs and X-Ds. The LAB is shallow (60–100 km) in Phanerozoic eastern Australia and deepens toward western cratonic regions (120–200 km). A thick lithosphere (170–200 km) with significant radial anisotropy but minimal S-velocity reductions is observed beneath central Australia. MLDs in cratonic regions are detected at three distinct depths (from 60 to 130 km), with either negative or positive S-velocity changes depending on the tectonic setting. X-Ds, characterized by velocity increases beneath the LAB, are detected at multiple depths (∼170 km, 220–270 km, and ∼310 km), commonly associated with the weakening of radial anisotropy underneath. The shallowest X-D (∼170 km) is found mainly beneath eastern Australia and is likely influenced by thermal effects in the asthenosphere, while deeper X-Ds may correspond to the Lehmann discontinuity or phase transitions of pyroxene. These findings provide a comprehensive view of the upper mantle discontinuities beneath Australia, offering new insights into the tectonic evolution of the Australian continent.

1. Introduction

Continental upper mantle discontinuities provide keys to unravel Earth's tectonic history and present-day mantle dynamics. Surface-wave tomography has been a particularly powerful tool for reconstructing large-scale seismic images of the upper mantle, enhancing our understanding of the lithosphere and asthenosphere systems in both continental and oceanic regions, which are closely linked to the forces driving plate motions (e.g., Yoshizawa, 2014; Isse et al., 2019; Yoshida and Yoshizawa, 2020). In addition, the receiver function method, which is effective in detecting seismic discontinuities beneath seismic stations, has recently revealed the enigmatic mid-lithospheric discontinuity (MLD) beneath the cratonic lithosphere, along with the lithosphere-asthenosphere boundary (LAB) (e.g., Rychert and Shearer, 2009; Liu et al., 2020; Kind et al., 2020). The MLD may reflect the ancient evolutionary process

*Corresponding author
tarumi.kotaro.jp@gmail.com (K. Tarumi)
ORCID(s): 0009-0002-9030-5408 (K. Tarumi); 0000-0003-2282-3748 (K. Yoshizawa)
https://twitter.com/<@mil\protect\T1\textunderscoreglobalseis> (K. Tarumi)

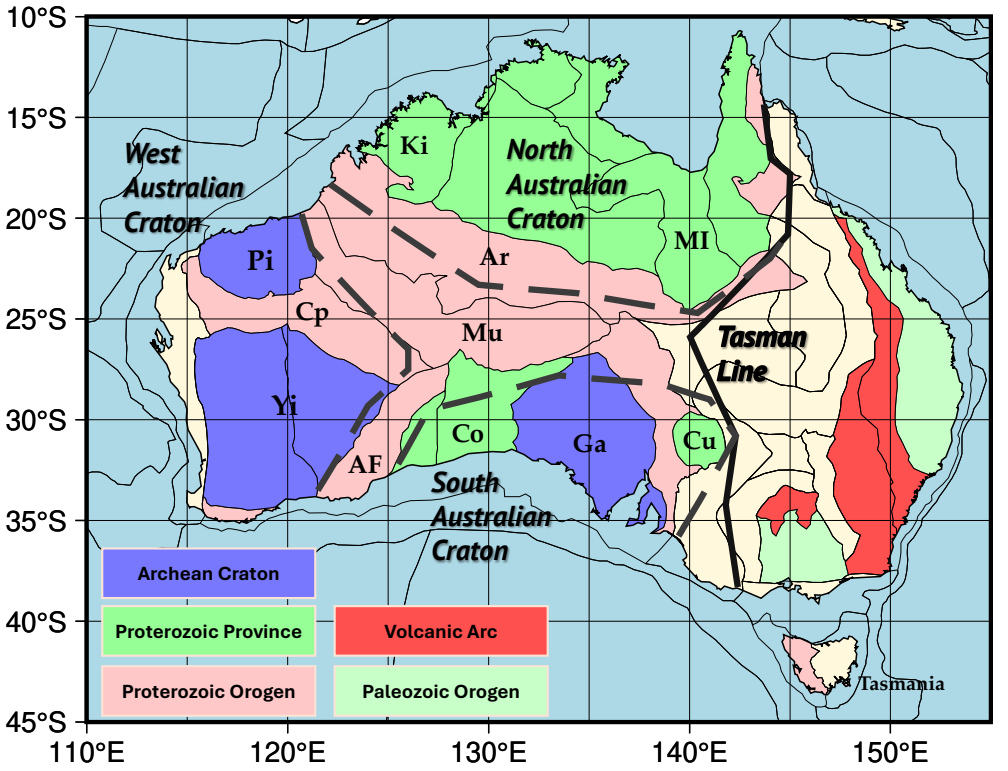


Figure 1: A tectonic map of the Australian Continent. Black solid and dashed lines delineate the boundaries of the major cratonic blocks (West, North, and South Australian Cratons) and the Tasman line. The boundaries of tectonic provinces are adapted from Hasterok et al. (2022) to reflect the local geological setting. The map highlights major tectonic provinces, including AF (Albany-Fraser belt), Ar (Arunta block), Co (Coompuna Province), Cp (Capricorn Orogeny), Cu (Curunamoa Craton), Ga (Gawler Craton), Ki (Kimberley Block), MI (Mount Isa Block), Mu (Musgrave Block), Pi (Pilbara Craton), and Yi (Yilgarn Craton).

of stable cratonic regions, while the LAB may be affected by the present-day plate motion and mantle flow. Therefore, it is essential to simultaneously capture the distributions and characteristics of both the MLD and LAB.

The upper mantle discontinuities beneath Australia provide critical insights into the formation and deformation of the continental lithosphere over Earth's history. The Australian continent was assembled during the mid-Proterozoic (1300–1000 Ma) through the amalgamation of three cratonic blocks: the West, North, and South Australian Cratons (Figure 1). A suture zone exists between the three cratonic blocks, which underwent multiple orogenic events, culminating in the Alice-Springs Orogeny ($\sim$ 400 Ma). The present Australian continent is characterized by western and central cratonic areas juxtaposed with the eastern Phanerozoic orogenic zone (Figure 1). Investigating the upper mantle discontinuities across Australia offers valuable insights into the evolutionary process shaping the continent.

The upper mantle discontinuities beneath Australia, including the Lithosphere-Asthenosphere Boundary (LAB), have been extensively investigated through various seismological and petrological approaches over the past several decades (e.g., Hales et al., 1980; Revenaugh and Jordan, 1991; Fishwick et al., 2008; Ford et al., 2010; Chen et al.,

2021b; Sudholz et al., 2024). Owing to the continuous efforts in expanding broadband seismic networks across the continent, including permanent and temporary stations (e.g., Rawlinson and Kennet, 2008; van der Hilst and Kennett, 1993), a number of 3-D shear velocity models have been proposed primarily based on surface wave tomography, providing clues of the Australian lithosphere-asthenosphere system (e.g., Fishwick et al., 2008; Kennett et al., 2013; Yoshizawa, 2014; Magrini et al., 2023). These studies reveal that the Australian LAB rapidly deepens from the eastern orogenic zone (50–100 km depth) to the cratonic areas in central and western Australia (around 120–200 km depth). However, surface waves are inherently less sensitive to sharp structural changes due to their long wavelengths, resulting in limited vertical resolution. In contrast, receiver functions (RFs) are highly sensitive to the impedance contrast across seismic discontinuities, and have been used to investigate the Australian upper mantle discontinuities (Ford et al., 2010; Birkey et al., 2021; Chen et al., 2021b). Despite these efforts, the sparse distribution of permanent broadband stations (Figure 2 (a)) has hindered constraining the spatial distribution of seismic discontinuities beneath the Australian upper mantle.

Within the lithospheric depth, potentially sharp negative velocity jumps at multiple depths in cratonic areas have been observed in recent studies using S-wave receiver functions (S-RFs) (e.g., Ford et al., 2010; Birkey et al., 2021), although such depths are generally characterized by high-velocity anomaly in surface wave tomography. These enigmatic mid-lithospheric discontinuities (MLDs) in the Australian lithosphere have also been detected at multiple depths through other seismological approaches (Sun et al., 2018; Kennett and Sippl, 2018; Taira and Yoshizawa, 2020; Chen et al., 2021b), suggesting that S-wave velocity changes across these MLDs do not always appear as negative shifts (e.g., Hales et al., 1980; Taira and Yoshizawa, 2020). Moreover, the characteristic properties of radial and/or azimuthal anisotropy may be varying across the MLDs (Yoshizawa and Kennett, 2015; Kennett et al., 2017; Taira and Yoshizawa, 2020; Chen et al., 2021b; Birkey and Ford, 2023). Although the elastic properties of MLDs are essential to understanding their physical nature, there remain many questions, such as the numbers, the spatial distributions, the style of velocity changes (positive/negative) across the MLDs, and their cause.

In addition to lithospheric interfaces, earlier studies (Hales et al., 1980; Drummond et al., 1982; Leven, 1985) identified deeper interfaces characterized by positive velocity jumps, detected in seismic waveforms recorded in northern and western Australia at depths around 200 and/or 325 km. Revenaugh and Jordan (1991) also suggested that the Australian upper mantle may host multiple discontinuities beneath the LAB. More recent work (Taira and Yoshizawa, 2020) combining P-RFs and surface wave dispersion data detected similar positive interfaces beneath five GSN stations in Australia, suggesting that one of these interfaces may correspond to the Lehmann discontinuity (Lehmann, 1961) and indicate the base of an anisotropic layer (i.e., asthenosphere) (Gaherty and Jordan, 1995; Taira and Yoshizawa, 2020). However, the nature and distributions of these enigmatic discontinuities beneath LAB (hereafter,

X-discontinuities or X-Ds) remain understood via localized analyses (Gaherty and Jordan, 1995; Taira and Yoshizawa, 2020).

In this study, we investigate the spatial distributions of seismic discontinuities in the Australian upper mantle through joint inversions using multimode surface-wave dispersions (SWDs) and P-wave RFs (P-RFs). At first, we estimate a large-scale topography map of the lithospheric base beneath Australia. Conventional LAB models (e.g., Kennett et al., 2013; Birkey et al., 2021) have been retrieved solely based on the information derived from either surface waves or receiver functions. Although Taira and Yoshizawa (2020) combined multimode SWDs with P-RFs to tackle the joint inversion analysis through Bayesian inference, their analysis was limited to localized applications. Here, we apply trans-dimensional joint Bayesian inversions to large data sets of broadband permanent and temporary stations across Australia, proposing an updated map of lithospheric thickness.

Additionally, we investigate the distribution and elastic properties of enigmatic MLDs and X-discontinuities (X-Ds). Previous MLD findings (Hales et al., 1980; Sun et al., 2018; Taira and Yoshizawa, 2020; Birkey et al., 2021, e.g.,) have been challenging to make a unified interpretation of these discontinuities due to inconsistencies in the nature of shear velocity changes and the presence of multiple interfaces. These discontinuities may offer potential insights into the past tectonic processes and present-day mantle dynamics (e.g., Srinu et al., 2021; Hua et al., 2023; Boyce et al., 2024). This study compiles the joint inversion results from numerous broadband stations in Australia to present new seismological evidence for the MLDs and X-Ds along with a revised lithospheric base model, providing a comprehensive discussion of their characteristics and plausible origins.

2. Data

This study employs multimode surface wave dispersions (SWDs) of Rayleigh and Love waves, derived from phase speed maps by Yoshizawa (2014), along with P-to-S receiver functions (P-RFs), following the methodology outlined in Tarumi and Yoshizawa (2025).

Our objective is to detect and image seismic discontinuities throughout the upper mantle above the mantle transition zone ($<$ 400 km). Taira and Yoshizawa (2020) demonstrated that the multimode SWDs significantly enhance the resolution of deep upper mantle SH-wave structure (i.e., radially anisotropic S-wave structures) since Love wave overtones are particularly sensitive below 200 km (Yoshizawa and Ekström, 2010, e.g.,). Thus, the use of multimode SWDs is essential for this analysis. Using high-resolution phase speed maps (Yoshizawa, 2014) enables us to explore the relationship between radial anisotropy and upper mantle discontinuities. Examples of multimode phase speed maps of Rayleigh and Love waves are shown in Figure S1.

For receiver functions analysis, we utilized 32 permanent stations and 86 temporary stations across the Australian continent (Figure 2 (a)). For permanent stations, we applied azimuth-dependent P-RFs using the signal-processing

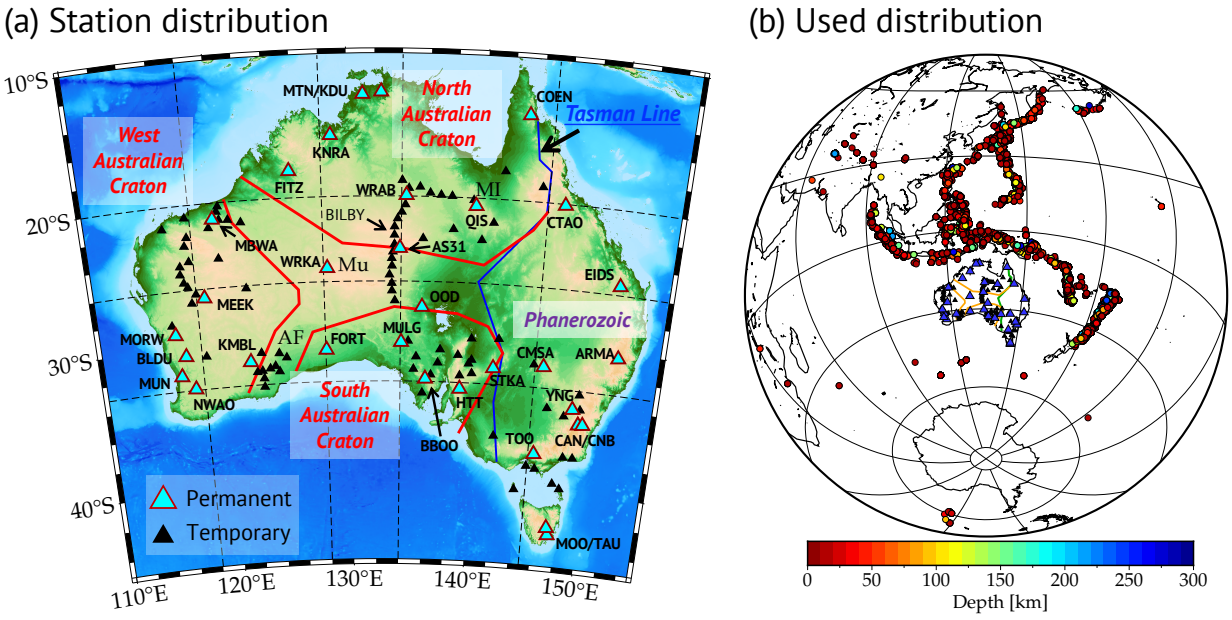


Figure 2: (a) Map of the study area showing employed stations. Cyan and black triangles indicate permanent and temporary stations, respectively, with permanent station names labeled. All station names are shown in Figure S2. Red lines represent the cratonic margins of the North Australian Craton (NAC), the South Australian Craton (SAC), and the West Australian Craton (WAC). The blue line denotes the Tasman Line, the geological boundary between the cratonic and eastern Phanerozoic regions. The Musgrave Province, the Mt. Isa Block, and the Albany-Fraser Belt are labeled as Mu, MI, and AF, respectively. Dashed lines represent cross-section paths shown in Figures 5, 6, 7, S6, and S7, along S20°, S26°, S33°, E118°, E128°, E134°, and E145°. (b) Map of event distributions used in receiver function analyses. Blue and black triangles present permanent and temporary stations. Colored circles indicate seismic events, while yellow and green lines are the major tectonic boundaries, the same as (a).

approach described in Tarumi and Yoshizawa (2025). Due to the shorter observation periods of temporary stations, we adjusted the data selection criteria accordingly. The employed events are shown in Figure 2 (b).

Examples of resultant P-RFs for permanent stations are shown in Figure 3, and the distributions of employed events for each station are shown in Figure S3. All stations exhibit clear azimuthal dependencies, particularly COEN (Figure 3 (a)), located at the northeastern tip of the continent (Figure 2). Figure S4 shows the corresponding short-period receiver functions for the same stations as in Figure 3, indicating the robustness of the main signals even at shorter-periods, despite contamination from multiple reverberations and scattered phases. At FORT (Figure 3 (c)), remarkable differences between low- and high-frequency datasets are observed, aligning with a previous RF study (Ford et al., 2010). The P-wave reflectivity profile at AU.FORT reveals intense reflection phases from shallow structure (i.e., the crust or sedimentary layers) (Kennett, 2015), with multiple phases that are weaker in the lower frequency profiles, consistent with our P-RF dataset (Figure 3).

In addition to permanent stations, we incorporated temporary stations deployed since 1993, including Skippy (van der Hilst and Kennett, 1993), QUOLL (Kennett et al., 1999), WA Cratons (Kennet, 2000), TASMAL (Kennett,

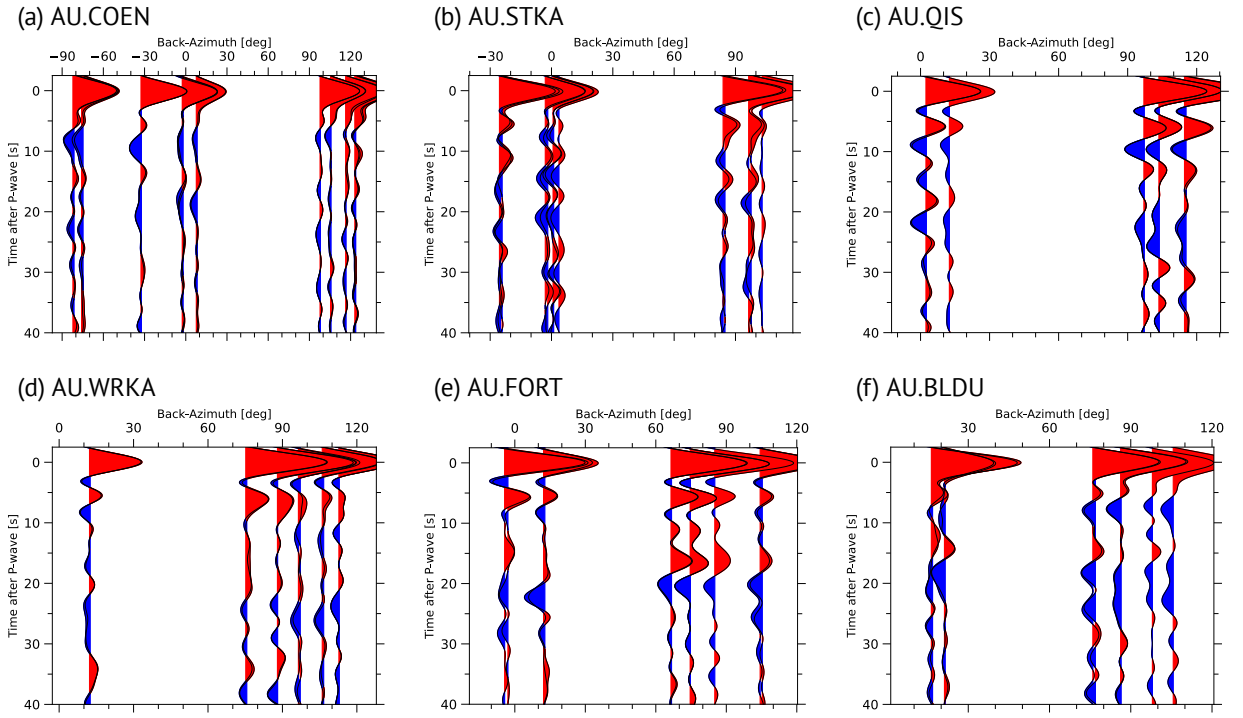


Figure 3: Examples of azimuth-dependent P-RFs for six permanent stations: (a) AU.COEN, (b) AU.STKA, (c) AU.QIS, (d) AU.WRKA, (e) AU.FORT, and (f) AU.BLDU. Positive and negative phases in P-RFs are shaded in red and blue, respectively.

2003), CARPA-Linkage (Reading and Kennett, 2005), SOC-Southern Craton (Fontaine and Kennet, 2007), BILBY (Rawlinson and Kennet, 2008), Bass Strait (Reading and Rawlinson, 2011), and Albany-Fraser Experiment (Tkalčić et al., 2013). Data processing for temporary stations was nearly identical to that for permanent stations. However, due to the shorter operation periods (1-2 years), we relaxed the criteria on epicentral distance and back-azimuth ranges of seismic events to better detect discontinuity depths. Thresholds for the cross-correlation selection (Tkalčić et al., 2006, 2011) were reduced to 0.7 for 0.03–0.2 Hz and 0.6 for 0.03–0.5 Hz to retain more traces in the stacking process, as visualized in Figure S5. For continental-scale discontinuity mapping, we applied lower weighting factors to temporary stations compared to permanent stations.

Figure 4 presents the stacked Ps receiver functions obtained from BILBY (Rawlinson and Kennet, 2008). The general P-RF characteristics are similar to Sippl (2016), especially the Moho-converted phases, which appear as positive signals at around 5–6 seconds. Later phases exhibit continuous changes across longitude and latitude, likely reflecting upper mantle heterogeneity. Although local azimuth-dependent variations around individual stations cannot be extracted in temporary stations due to the limitation of the observation period, the temporary stations provide valuable complementary data (locally averaged S-wave model) to supplement the sparse distribution of permanent stations (Figure 2).

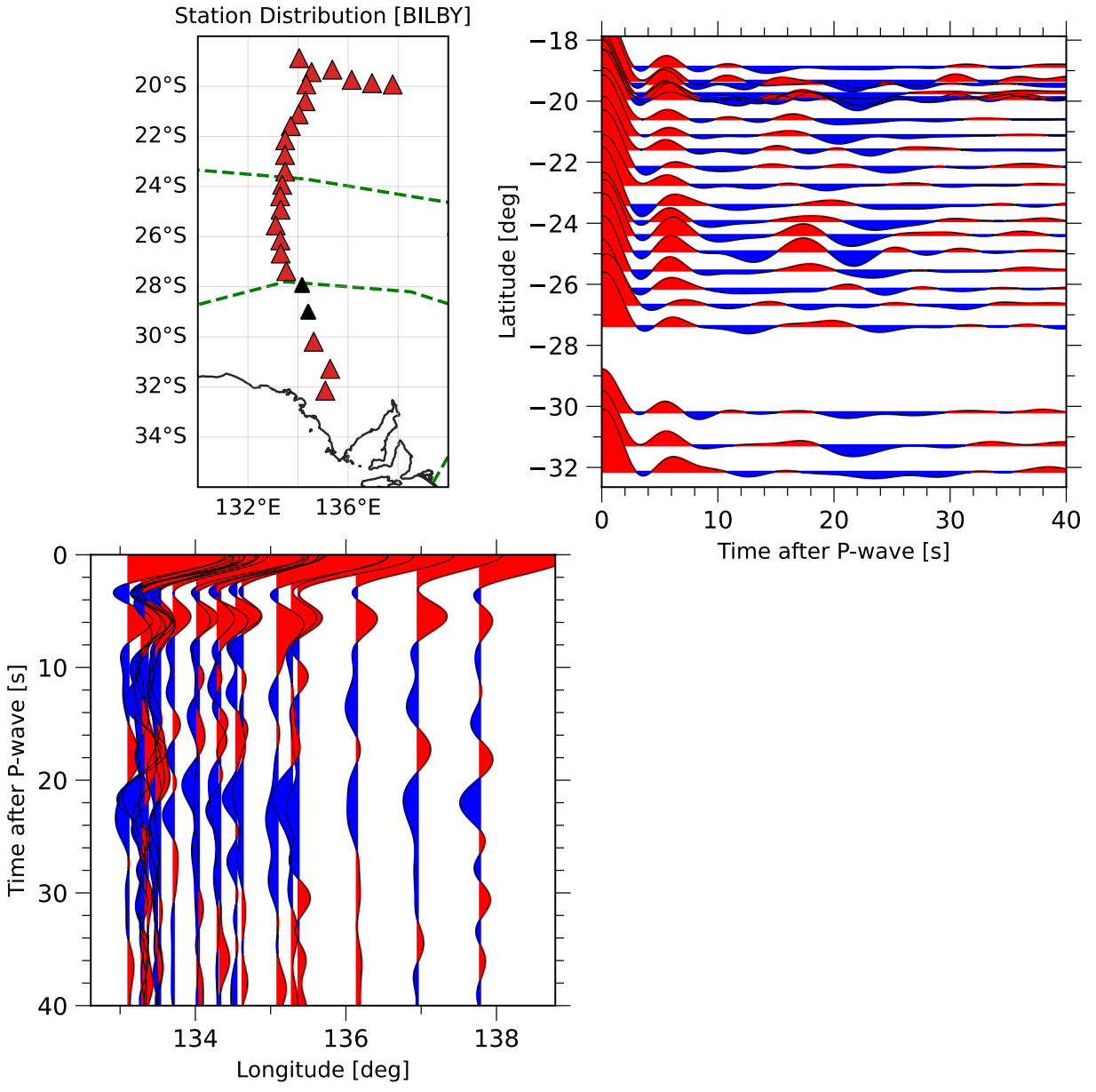


Figure 4: Stacked P-RFs observed at the BILBY array (Rawlinson and Kennet, 2008). The top left panel displays a map of the BILBY stations (triangles), with major tectonic boundaries (green dashed lines) of the NAC and SAC. Red triangles indicate stations that meet the data selection criteria, as described in the main text. The top-right panel represents the Ps receiver functions sorted by latitude, and the bottom panel by longitude.

3. Methods for discontinuity detection and mapping

3.1. Trans-dimensional Bayesian inversion and discontinuity detections

To jointly invert multimode SWDs and P-RFs, we employed the hierarchical trans-dimensional Bayesian inversion scheme (Bodin et al., 2012; Calò et al., 2016; Taira and Yoshizawa, 2020; Tarumi and Yoshizawa, 2025). The Bayesian

inference enables us to represent the model parameters as probability density functions, allowing us to treat the number of parameters and the data uncertainties as unknown parameters in the optimization process, which have generally been predefined as a priori parameters in conventional linearized inversions. This advanced inversion technique has recently been widely used in joint inversions involving multiple datasets (e.g., Kim et al., 2016; Calò et al., 2016; Akuhara et al., 2023). While such trans-dimensional inversion is computationally demanding, we employed the parallel tempering method (Sambridge, 2014) to expedite the convergence of parameter search, as in Taira and Yoshizawa (2020). Detailed descriptions of the formulations and workflows employed in this study are provided in Tarumi and Yoshizawa (2025).

We retrieved radially anisotropic S-wave speed models, including discontinuity depths, using the multimode SWDs and P-RFs. After inversions, we computed isotropic S-wave speed using the Voigt average of the inverted SV and SH velocities, $V_{S_{iso}} = \sqrt{\frac{2V_{SV}^2+V_{SH}^2}{3}}$, and radial anisotropy, $\xi = \left(\frac{V_{SH}}{V_{SV}}\right)^2$, following Yoshizawa (2014).

Using the radially anisotropic models, at first, we determined the Moho and LAB based on vertical changes in shear wave speed. When a low-velocity zone and/or a shear velocity drop were absent or unclear, we defined the lithospheric base using radial anisotropy (ξ) following Plomerová et al. (2002). In estimating the lithospheric base, we incorporated the Lithosphere-Asthenosphere Transition (LAT) defined by Yoshizawa (2014). The LAT is characterized by the vertical gradient of S-wave velocity from the multimode surface-wave tomography model, with the upper and lower bounds derived from the negative peak of the S-wave gradient and the depth of minimum velocity, respectively, indicating potential lithospheric thickness with a gradual transition from the lithosphere to asthenosphere.

After defining the crust and mantle lithosphere, we identified Mid-Lithospheric Discontinuities (MLDs) within the mantle lithosphere and X-discontinuities (X-Ds) beneath the LAB. The following criteria were used to define these discontinuities:

- Moho: The location of maximum S-wave speed increase around the reference Australian Moho depth (Kennett et al., 2023).
- Lithospheric base: If the S-wave speed is below 4.7 km/s near the LAT, the LAB is marked by a 0.04 km/s S-velocity drop. When the low-velocity zone is unclear (e.g., southern NAC and the suture zone), we used a depth with a rapid increase in radial anisotropy to define the lithospheric base (Plomerová et al., 2002).
- MLDs: Depths with an S-velocity change of over $\pm$ 0.02 km/s above the LAB or the upper bound of LAT.
- X-Ds: Positive S-velocity jumps of more than 0.04 km/s below the lithospheric base.

In this study, we did not impose any criteria on radial anisotropy when identifying MLD and X-Ds to allow an unbiased analysis of radial anisotropy variations across these discontinuities.

3.2. Regional-scale mapping process of seismic discontinuities

For permanent stations, after detecting interfaces based on the definition described above, we computed azimuth-dependent conversion point depths to map lateral changes in seismic discontinuities around each station. Our approach with azimuth-dependent P-RF analysis employed for the permanent stations allows us to estimate local lateral variations in seismic discontinuities, as described in Tarumi and Yoshizawa (2025). However, as our current scope focuses on mapping upper mantle discontinuities at a continental scale, we compute a representative interface depth for each station.

To determine the representative LAB depth at each permanent station, we computed a weighted average of conversion points and a weighted isotropic S-wave reductions across the LAB. When the lithospheric base is better identified by radial anisotropy, the mean of the selected depths is used instead. Similarly, we determined representative Moho depths with weights based on S-velocity jumps. For temporary stations, discontinuity depths are estimated using the same criteria as described in the previous subsection. In the case of MLDs and X-Ds, we conduct an additional clustering analysis, which will be explained in detail in the next section.

We then compare these estimated conversion point depths with the surface-wave tomography model (Yoshizawa, 2014) in Figure 5 and examine azimuthally-averaged posterior distributions and discontinuity depths for permanent stations in Figure 6. This approach effectively captures both the large-scale features of the Australian upper mantle interface and their lateral variations.

3.2.1. Conversion points vs. tomography model

Figure 5 shows the distribution of conversion points (CPs) overlaid on cross-sectional tomographic models of isotropic S-wave speed and radial anisotropy (Yoshizawa, 2014), with the upper and lower bounds of the LAT (Yoshizawa, 2014) superimposed.

LAB-related CPs are generally distributed in the low-velocity zone and within the LAT, with green and white dots situated between the white and red dashed lines (Figure 5). In Phanerozoic eastern Australia and the West Australia Craton (WAC), the LAB CPs correspond to the transition depths between high- and low-velocity zones (Figure 5 (a, b, c, d, f)). At these depths, radial anisotropy (ξ) increases gradually, especially in southeastern and northeastern Australia (Figure 5 (a, c, f)).

In the southern part of North Australian Craton (NAC) and the suture zone (Figure 5 (a, b, e)), although the LAB signature in shear velocity changes are unclear, CPs at the lithospheric base (white dots) align with the depth of relatively lower-velocity anomaly in the tomographic model (Yoshizawa, 2014). Radial anisotropy sharply increases across these CPs, indicating that our definition of the lithospheric base can be a reasonable choice in the lithosphere-asthenosphere system beneath cratonic areas with weak S-velocity drop.

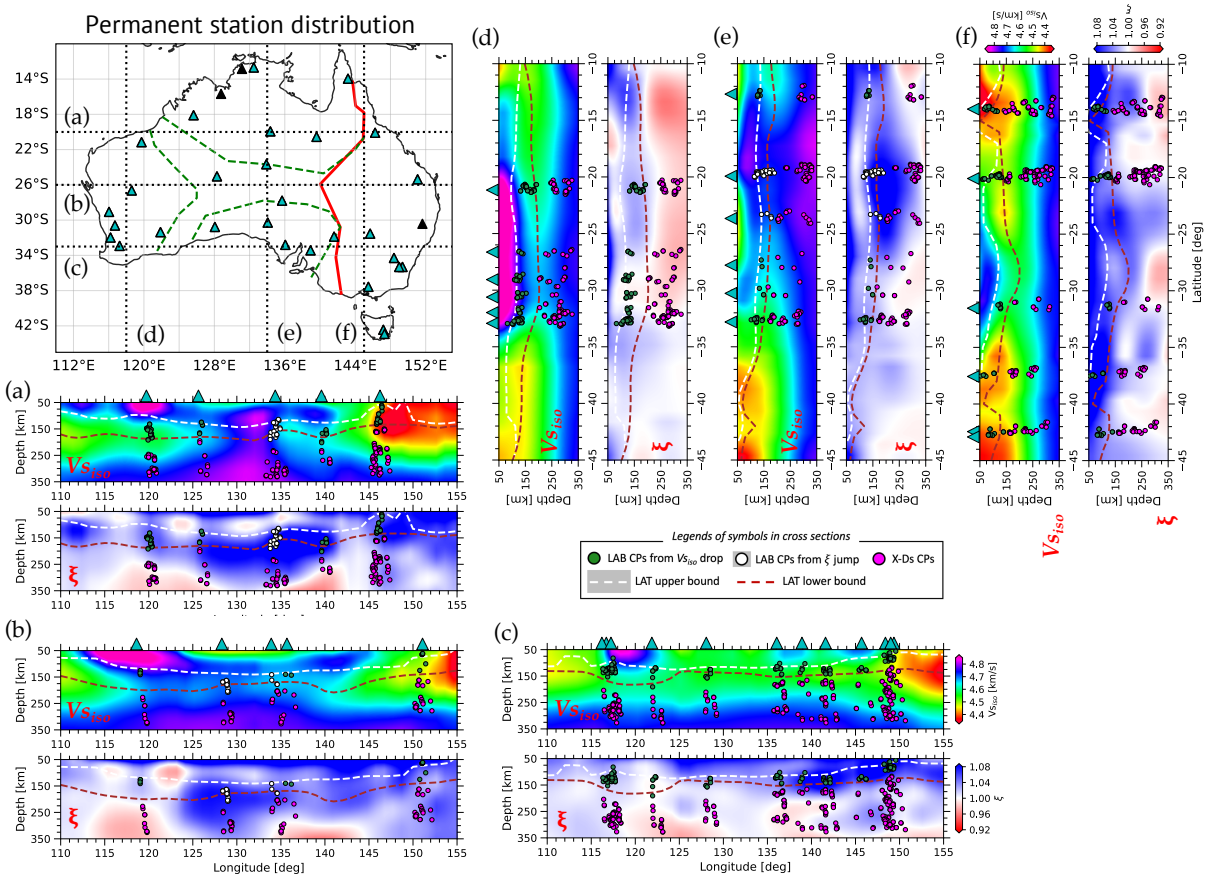


Figure 5: Cross-sectional view of conversion points for the LAB and X-Ds. The top-left panel shows the distribution of employed permanent stations (cyan triangles), with major tectonic boundaries and the Tasman Line drawn by green dashed and red solid lines, respectively. (a–c) E-W cross-sections of isotropic S-wave speed and radial anisotropy models reconstructed from multimode surface-wave tomography (Yoshizawa, 2014), with the upper and lower bounds of the LAT indicated by white and red dashed lines. Green and white dots represent LAB (or lithospheric base) conversion depths from individual inversion results, while magenta dots indicate X-Ds conversion points. (d–f) Same as (a–c), but for N-S cross-sections.

X-D CPs (magenta dots) are scattered at various depths where S-wave velocity increases with depth, forming clusters based on tectonic provinces. Along S33° (Figure 5 (c)), from E135° to E150°, three X-D clusters appear at around 140–170 km, 240–260 km, and 280–325 km. At the shallowest depth, radial anisotropy notably decreases, particularly in eastern Australia and the SAC (Figure 5 (c)), as also shown in radially anisotropic S-wave velocity profiles (Figure 6). Although shallow X-D clusters are absent in some regions, the relationship between X-D CPs and radial anisotropy is observed across other cross-sections, with depth variations depending on the tectonic province.

3.2.2. Azimuthally-averaged 1-D radially anisotropic S-wave models

Figures 6 and S6 present azimuthally-averaged posterior densities and estimated Moho and LAB depths for permanent stations within 2° along S33°, S20°, and S26°. Figures 7 and S7 provide similar information for N-S

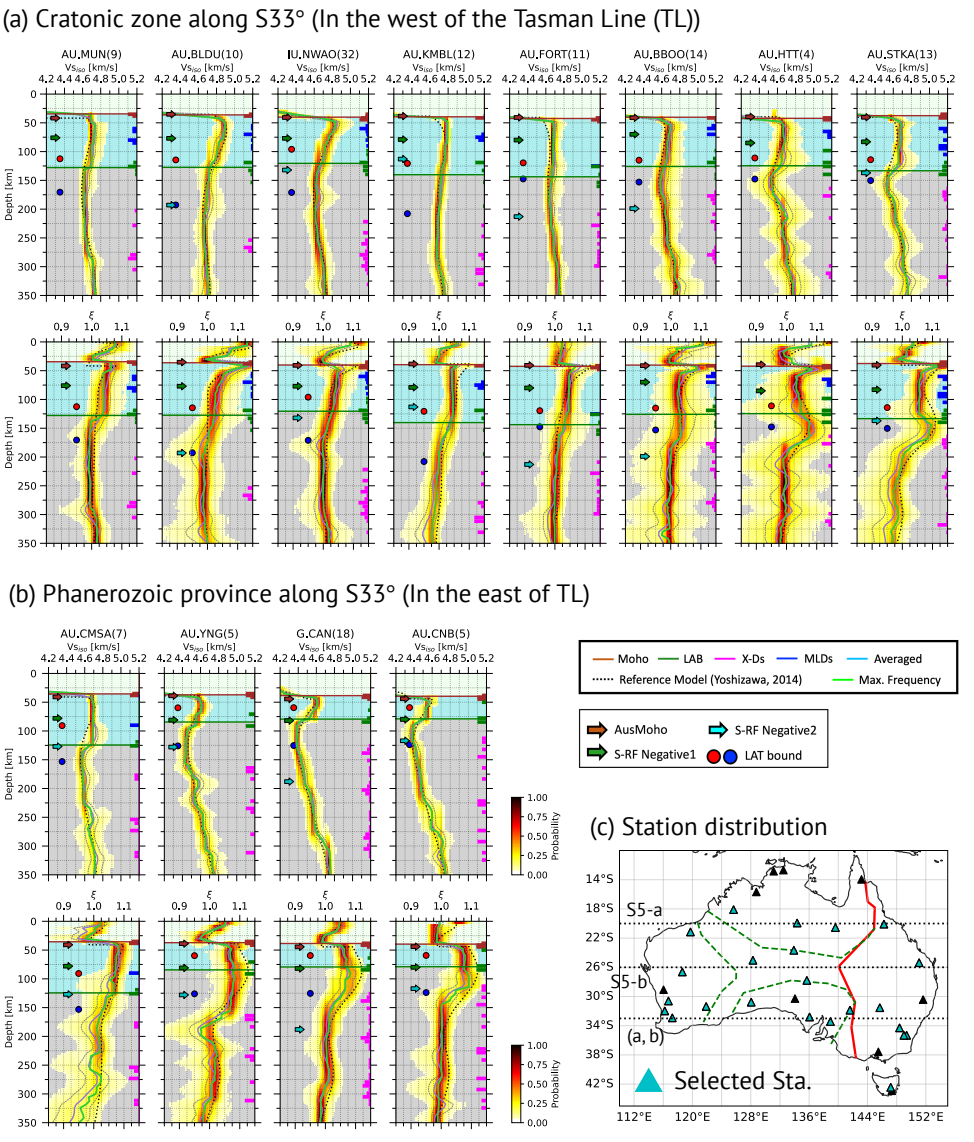


Figure 6: Azimuthally-averaged 1-D posterior densities of radially anisotropic S-wave models for permanent stations along S33°. (a) Probabilistic models for stations located within the cratonic region, with station names and the number of inverted 1-D profiles (i.e., azimuth-dependent 1-D models) indicated above each panel, arranged from west to east. The upper and lower panels show vertical profiles of isotropic S-wave speed and radial anisotropy, with brown and green horizontal lines representing the weighted-average Moho and LAB depths, respectively. Light-green and light-blue shaded regions indicate the crustal and lithospheric zones. The rightmost colored bars display normalized histograms for the identified discontinuity depths. Boundary estimates and 1-D profiles from earlier studies are superimposed as colored arrows, circles, and black dotted curves, as displayed above (c). (b) Same as (a), but for stations in the Phanerozoic region (east of the Tasman Line). (c) Map showing the distribution of permanent stations, with cyan for selected stations and black for others. Black dotted lines represent locations at S20° , S26°, and S33° shown in Figure S6 (a, b).

cross-sectional stations along E118°, E128°, E134°, E145°, and E155°. Each radially anisotropic 1-D profile includes boundary estimates from AusMoho (Kennett et al., 2023), LAT (Yoshizawa, 2014), and negative S-RF phases (Birkey et al., 2021). Brown and green horizontal lines indicate the estimated azimuthally-averaged Moho and LAB (or

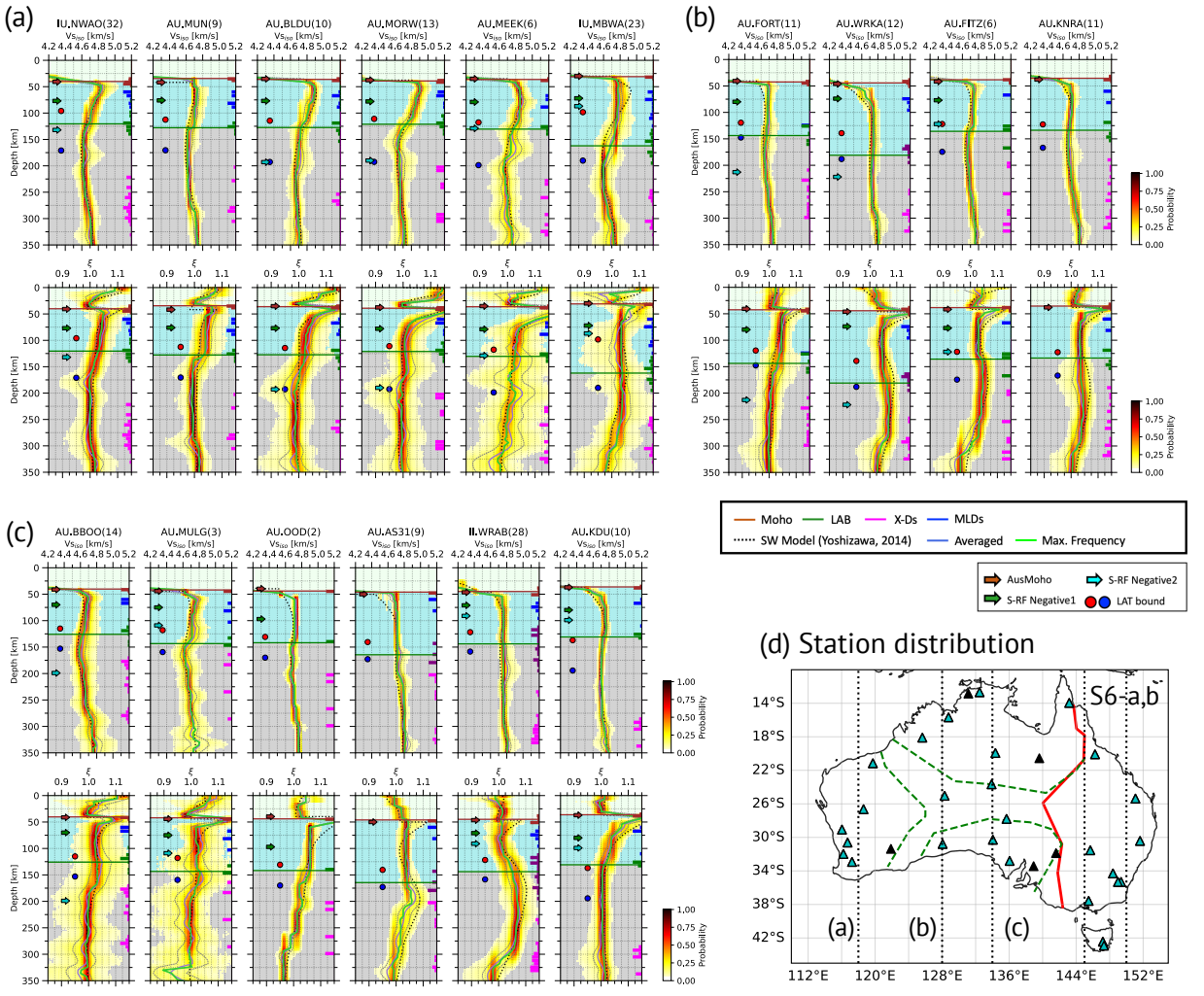


Figure 7: Same as Figure 6, but for the N-S cross-sectional views of 1-D profiles along E118° (a), E128° (b), and E134° (c), where the stations are arranged from south to north. Additional figures showing the same views along E145° and E155° are provided in Figure S7.

lithospheric base), while the colored bars on the right vertical-axis of each panel exhibit individual discontinuity depths derived from azimuth-dependent 1-D profiles. In this study, we consider the azimuth-averaged 1-D radially anisotropic S-wave speed models and the Australian lithospheric base.

Along the E-W cross-sectional profiles (Figures 6 and S6), lithospheric thickness (light-blue shaded area) gradually varies in the cratonic province (120–150 km), but thins rapidly toward eastern Australia (70–100 km). While azimuth-dependent LAB depths (leftmost green bars) mostly align with azimuthally averaged LAB depth (green horizontal lines), stations like MBWA and CTAO exhibit widespread distributions (Figure S6), indicating localized lateral variations in the LAB (as shown in Tarumi and Yoshizawa (2025)). In the suture zone, WRKA and AS31 stations reveal anomalously thick lithosphere, extending to 170–200 km depths (Figure 7 (b, c)).

The sharpness of the S-wave velocity drop varies by tectonic provinces. In eastern Australia and the eastern SAC (Gawler craton), significant shear wave reductions are observed at the azimuthally-averaged LAB (green horizontal lines), accompanied by a sharp increase in radial anisotropy (Figure 6), suggesting strong shear flow in the asthenosphere. To the contrary, the WAC shows moderate S-wave reductions and weak anisotropy (Figures 6 (a) and 7 (a)).

Profiles for WRKA, AS31, and WRAB, characterized by very thick lithosphere, exhibit a high-velocity zone (4.7–4.8 km/s) extending to a depth of 350 km from the average Moho (brown lines). Although no S-wave speed decrease is observed, radial anisotropy strengthens significantly ($\sim$ 10 %) below the lithospheric base. These features, corroborated by dense temporary stations from the southern NAC to the SAC (BILBY (Rawlinson and Kennet, 2008) in Figures 2 and 4) and the Albany-Fraser belt (ALFREX: Tkalčić et al. (2013)), likely reflect structural characteristics of the Australian cratonic suture zone and adjacent region, such as the southern NAC.

4. Seismic discontinuity maps beneath Australia

In this section, we compile the conversion depths for each station to estimate the spatial distribution of each discontinuity. Spatial interpolation provides insights into the large-scale structure of upper mantle discontinuities, while the station-based conversion depth maps reveal localized variations that enhance our interpretation.

For the Moho and the lithospheric base, the mapping strategy follows the straightforward approach described in Section 3.2. For X-Ds and MLDs, however, we performed clustering analyses before mapping to group the conversion points into three or four categories. The following subsections provide details of methodologies and the results of these clustering analyses.

4.1. Moho discontinuity

Regional-scale Australian Moho models have been developed in several studies (e.g., Kennett and Saygin, 2015; Birkey et al., 2021; Kennett et al., 2023; Magrini et al., 2023). In particular, Kennett et al. (2023) provided a comprehensive Australian Moho model (Figure 8 (a)) by integrating various geophysical observations, including reflection and refraction surveys and receiver function analyses.

Our resulting Moho map is shown in Figure 8 (c, d), with station-based Moho depths in (c) and their spatial interpolation in (d). Overall, our Moho model reveals deepening toward the central region from the continental margin (Figure 8 (c, d)).

In the Phanerozoic province, our model estimates the crustal thickness around 35 km, with locally deep Moho in southeastern Australia ($\sim$ 40–50 km near Canberra) and shallow Moho near Tasmania ($\sim$30 km) (Figure 8 (c, d)). Along the Tasman Line, marking the transition between cratonic and the Phanerozoic basement, the crust-mantle boundary

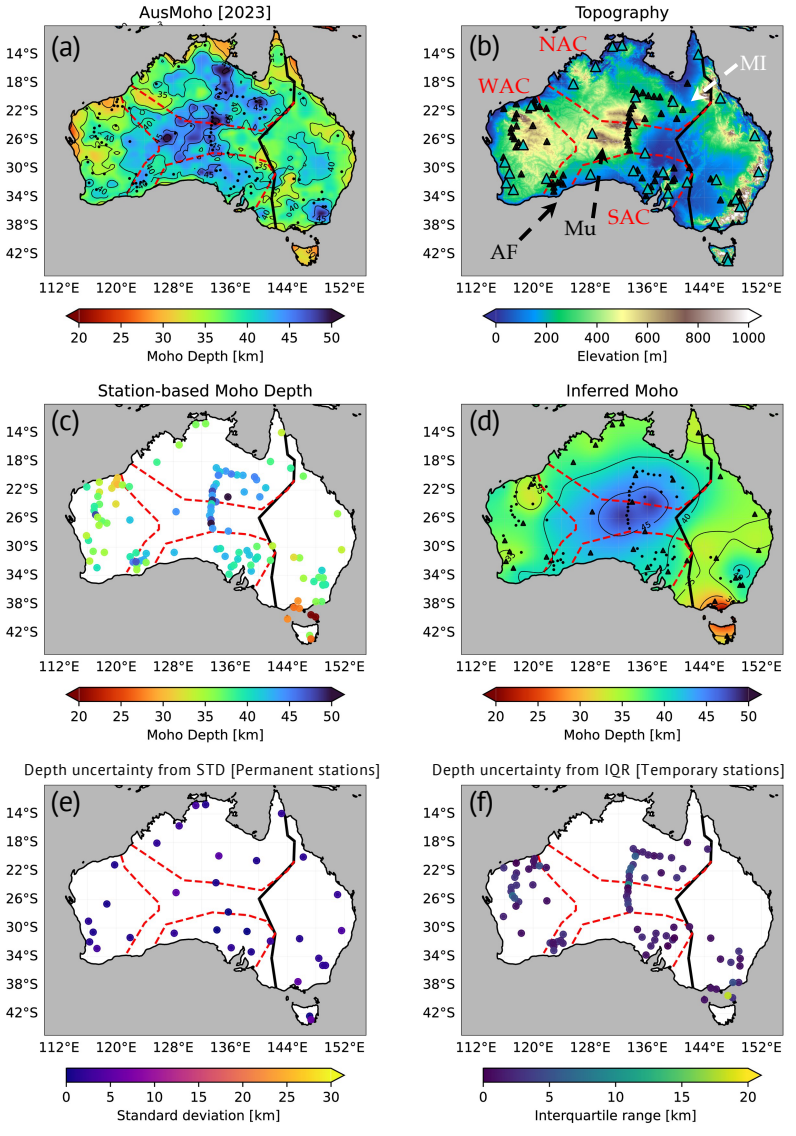


Figure 8: Map of the Moho discontinuity. Tectonic boundaries of WAC, SAC, NAC, and the Tasman Line are shown as red dashed and black solid lines in all panels. (a) The AusMoho model (Kennett et al., 2023), with black dots indicating the station locations used in this study. (b) Surface topography and station distributions. WAC: West Australian Craton, NAC: North Australian Craton, SAC: South Australian Craton, AF: Albany-Fraser orogenic belt, MI: Mount Isa Block, Mu: Musgrave Province. (c) Moho depths estimated at individual stations. (d) Spatially interpolated Moho depth map based on (c), with black triangles and circles representing permanent and temporary stations, respectively. Black contours denote depth intervals of 5 km. (e) Standard deviation of the Moho depths at permanent stations, derived from the azimuth-dependent conversion points. (f) Uncertainties of the Moho depth at temporary stations, estimated from the interquartile range (IQR).

shows rapid changes: the southern transition zone has a thinner crust (30–35 km), while the northern zone has a thicker crust (40 km).

In the cratonic regions, the Moho varies by tectonic province (Figure 8 (c, d)). The crust-mantle boundary is relatively flat at ∼ 45 km across the southern and central NAC, while the WAC shows greater variation. The Pilbara

craton has a thinner crust (∼ 30 km), whereas the Yilgarn craton has a thicker crust (35-40 km). In the cratonic suture zone, the Moho deepens to ∼ 50 km, with localized deepening extending beyond 50 km in the Alice-Springs Orogeny and the Musgrave Province.

Our model agrees with recent Moho models (Kennett et al., 2023; Magrini et al., 2023), showing overall features and localized crustal variations. Some discrepancies, such as in northern NAC, are likely due to station coverage. In central Australia and the Albany-Fraser belt (AF in Figure 8 (b)), localized deepening patterns also matched with the AusMoho model (Figure 8 (a); Kennett et al. (2023)) and receiver function studies (Sippl, 2016; Kennett and Sippl, 2018; Sippl et al., 2017).

Figure 8 (e, f) represents the compiled uncertainties of the estimated Moho depths. For permanent stations, we show the standard deviations of the azimuthally-varying conversion point depths at the Moho, derived from the azimuth-dependent P-RFs (Figure 8 (e)). These deviations can be interpreted not only as measures of uncertainty in the estimated depth but also as indicators of azimuthal variations in Moho depth around each permanent station. For temporary stations, the uncertainties are quantified using the interquartile range (IQR) of the Moho depths derived from the posterior distributions of the inversion. Overall, the uncertainties in the estimated Moho depths are on the order of a few kilometers (Figure 8 (e, f)).

4.2. Base of lithosphere

The thickness of the Australian lithosphere has been explored through various approaches (e.g., surface-wave tomography; receiver functions; travel-time tomography), yielding consistent large-scale models that show lithospheric thickening from the eastern Phanerozoic provinces to the western cratonic areas (e.g., Fishwick et al., 2008; Kennett et al., 2013; Yoshizawa, 2014; Davies et al., 2015; Magrini et al., 2023; de Laat et al., 2023). In this study, we combined multimode SWD with P-RFs, sensitive to seismic interfaces, to propose an updated model of lithospheric thickness. Figure 9 presents the resulting lithospheric base model, displaying station-based conversion depths and their spatial distribution across Australia in (a) and (b).

In the younger orogenic zone of eastern Australia, the LAB is shallow (60–100 km), thickening rapidly westward toward the Precambrian cratonic areas (∼120 km). The northeastern lithosphere, estimated at ∼100 km thick, shows a sharp lateral change from east to west (Figure 9), as also evidenced by azimuth-dependent inversion results at the CTAO station (Tarumi and Yoshizawa, 2025). In southeastern Australia, including Tasmania (S45°–S22°), the LAB depth is around 80 km, thickened gradually toward the SAC margin (Figure 9).

Beneath southeastern Australia (around S33°/E144°), a somewhat thicker lithosphere (100–120 km) is observed, which is similar to the cratonic lithosphere (Figure 9). In addition, the S-wave speed in this layer exceeds 4.6 km/s, equivalent to that observed in the SAC (Figure 6), suggesting that this area may represent a cratonic-style lithosphere

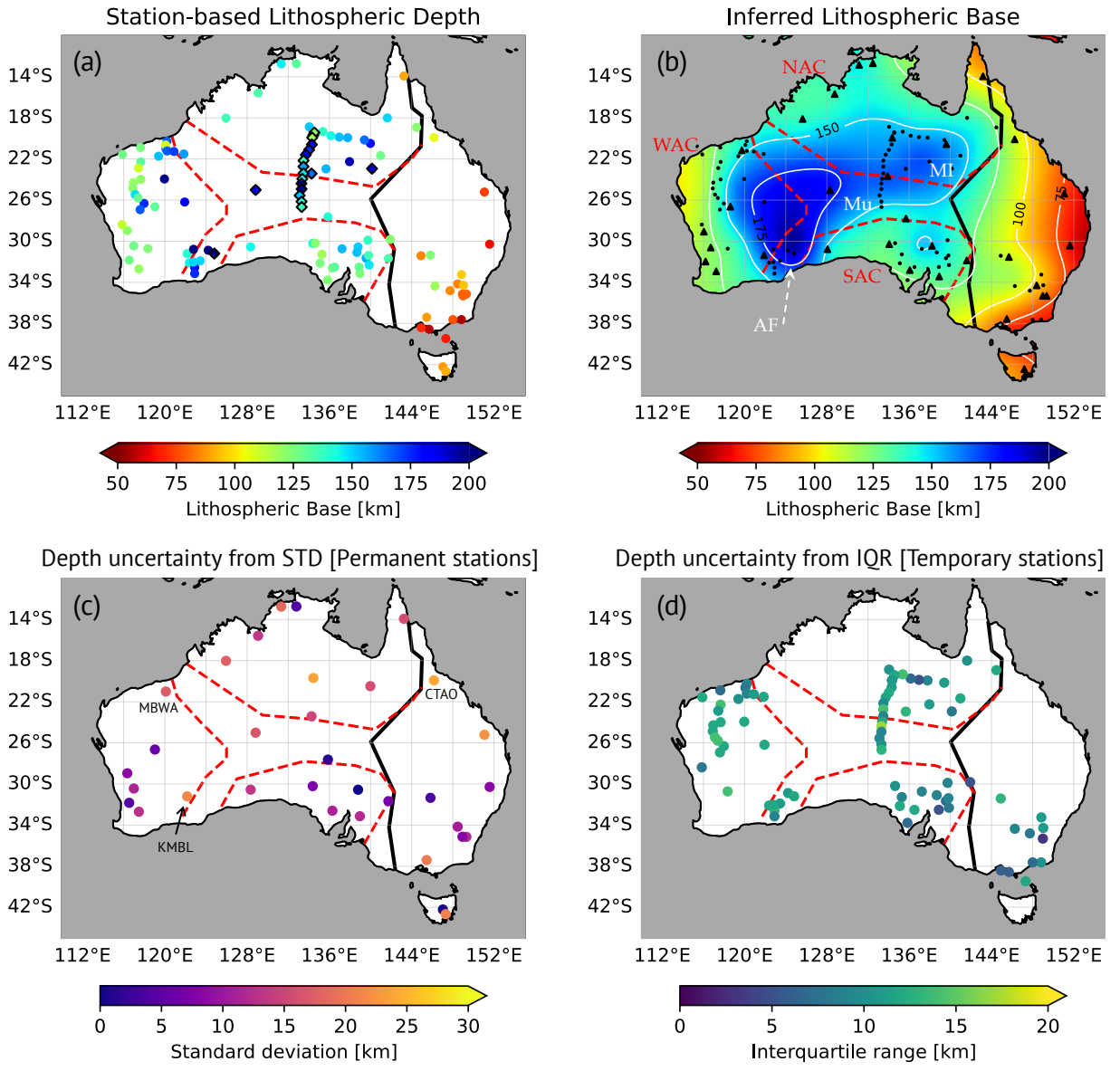


Figure 9: Map of lithospheric thickness. (a) Same as Figure 8 (a), but showing the depth of the lithospheric base. Diamonds indicate locations where the lithospheric base was identified from radial anisotropy, particularly in regions where S-wave reductions are unclear. (b) Same as Figure 8 (d), but for lithospheric thickness. Thin white contours represent depth intervals of 25 km. (c, d) Same as Figure 8 (e, f), but for the lithospheric base. WAC: West Australian Craton, NAC: North Australian Craton, SAC: South Australian Craton, AF: Albany-Fraser orogenic belt, MI: Mount Isa Block, Mu: Musgrave Province.

rather than typical Phanerozoic lithosphere (Simons et al., 2002; Fishwick et al., 2008; de Laat et al., 2023). This observation implies that the surface geological trace of the Tasman Line may not necessarily represent its subsurface extension in the mantle. Still, a nearby temporary station (7I.TL16 in Figure S2(b)) indicates a shallower LAB (about 100 km) in this area (Figure 9 (a)), consistent with the trend in the Moho model (Figure 8 (a, c)), suggesting complex crustal and lithospheric structures in the transition area between Phanerozoic and cratonic provinces.

In contrast, the lithosphere within major cratonic blocks is relatively flat at 120–150 km and deepens to ∼200 km in central Australia (Figure 9). The LAB in the SAC is notably flat at ∼130 km, with a slight deepening (∼150km) just north of the Gawler craton (Figure 9). Meanwhile, the lithospheric thickness in the WAC and NAC varies laterally toward the cratonic suture zone.

In the western WAC, a flat LAB at ∼120 km deepens gradually toward the cratonic suture zone. Lithosphere thickening is observed at the edge of the Archean Yilgarn and Pilbara cratons (Figure 9 (a)), reaching 170–200 km depths. The southern NAC features a thicker lithosphere than the WAC and SAC, estimated at 150–170 km depths (Figure 9). Based on station-based LAB depths (Figure 9 (a)), localized deepening of the lithospheric base (180–200 km) is evident in the southern NAC and the Mount Isa Block (MI in Figure 1).

In the suture zone, particularly the Musgrave province, we observe evidence of anomalously thick lithosphere reaching 170–200 km (Figure 9 (a)). Another area of thickened lithosphere appears at the boundary between the WAC and SAC, within the mid-Proterozoic orogenic zone (AF: the Albany-Fraser orogenic belt), also showing localized variations in lithospheric thickness.

The overall pattern in Figure 9 suggests a deepening LAB from eastern to cratonic regions in central and western Australia, consistent with previous lithosphere models based on surface-wave tomography (Fishwick et al., 2008; Kennett et al., 2013; Yoshizawa, 2014; Magrini et al., 2023). Although lateral resolution is still limited due to poor station coverage, particularly in northern NAC, our LAB model (Figure 9 (a)) involves some localized features derived from joint analysis using multimode SWDs and P-RFs.

Figure 9 (c, d) shows the depth uncertainties of the lithospheric base, corresponding to those for the Moho in Figure 8 (e, f). Individual uncertainties for the temporary stations are generally less than 15 km (Figure 9 (d)), which is also similar to the individual inversion results for most permanent stations. Still, relatively larger standard deviations (computed from the azimuth-dependent conversion depths) are observed for some permanent stations located near major tectonic boundaries, such as CTAO, MBWA, and KMBL, likely reflecting the significant lateral variations in lithospheric structure under these stations.

4.3. X-discontinuities

Prior to mapping, we conducted a clustering analysis. As explained in Section 3.2, the X-Ds form depth-dependent clusters that vary with tectonic province (Figure 5). We applied k-means clustering to group the estimated X-Ds based on five parameters: horizontal location (longitude and latitude), depth, radial anisotropy, and the vertical change of radial anisotropy. For the k-means cluster analysis, the number of clusters, N_c, must be predefined. We tested two cases with $N_c = 3$ and 4, based on the depth distribution of the identified X-Ds (Figure 5), pre-clustering histograms, and silhouette scores. To preserve the physical meaning of each parameter, we did not standardize the input variables,

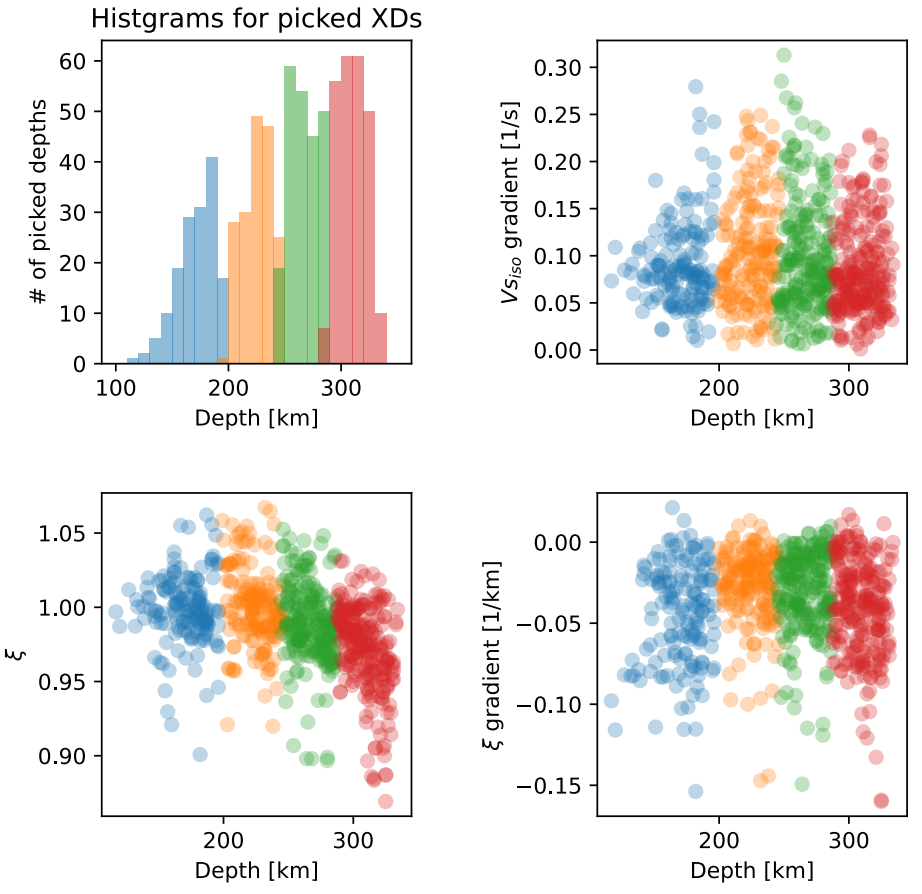


Figure 10: Results of the clustering analysis for the conversion points of X-Ds, with clusters numbered from 1 to 4 represented by blue, orange, green, and red. (a) Histograms of X-D depths for each cluster. (b, c, d) Relationship between shear wave velocity change, radial anisotropy, and vertical change in radial anisotropy.

although this is a common practice in statistical clustering analysis. For clarity, we mainly discuss the results for $N_c = 4$ in the main text, while the results for $N_c = 3$ are provided in Figures S9 and S10 in the Supplementary Material.

Figure 10 shows the results of clustering analysis. The primary factors in this analysis are the location and depths of the conversion points, as data standardization was not applied. Other model parameters, however, also correlate with depths, supporting the validity of our analysis. From Figure 10 (a), we identify four distinctive interfaces: 170km-D, 220km-D, 270km-D, and 310km-D.

For permanent stations, which include azimuth-dependent X-D estimates, we applied the same procedures used for the Moho and the lithospheric base, as described in Section 3.2. Specifically, after clustering, we computed a representative depth for each cluster at the permanent stations by averaging the depths of the conversion points within the same group, weighted by the magnitude of shear wave speed changes.

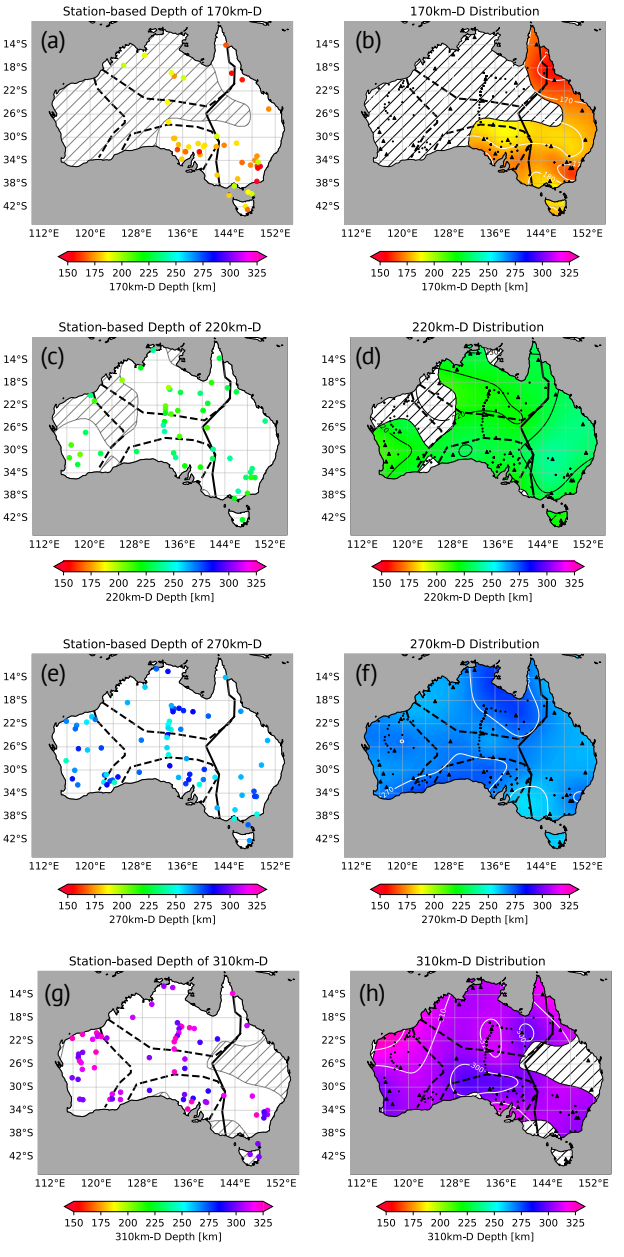


Figure 11: Maps of X-Discontinuities. (a, c, e, g) Same as Figures 8 (c) and 9 (a), but for the 170km-D, 220km-D, 270km-D, and 310km-D. Black solid and dashed lines represent the Tasman Line and cratonic boundaries, respectively. (b, d, f, h) Same as Figure 8 (d) and 9 (b), but for the 170km-D, 220km-D, 270km-D, and 310km-D. Thin black or white contours indicate a 10 km depth interval. In (a, b, c, d, g, h), shaded areas represent regions with unclear presence of discontinuity, as inferred from the normalized Gaussian kernel density explained in the text.

To determine the existence of an X-D quantitatively, we treated the conversion points in each cluster as a point cloud to calculate the normalized Gaussian kernel density, representing the probability of a Ps conversion from an X-D. Regions where this probability is less than 0.1 are defined as uncertain areas for an X-D.

The resultant maps for the four discontinuities beneath the LAB are displayed in Figure 11: panels (a, c, e, g) show the station-based distributions for each discontinuity, while panels (b, d, f, h) show spatially interpolated maps. Regions with insufficient data or large uncertainties are masked to indicate areas of low confidence in the X-D estimates. The associated depth uncertainties are shown in Figure S8. Figures S10 and S11 present corresponding maps to Figures 11 and S8, respectively, but for the case of three clusters ($N_c = 3$).

The 170-km discontinuity (170km-D), the shallowest X-D, is mainly observed in the eastern Phanerozoic province and the eastern SAC, with limited detection in the WAC and NAC (Figures 5 and 11 (a, b)). In northeastern and southeastern Australia, 170km-D lies at 150–170 km depth, gradually deepening to 170-190 km in the SAC, although this trend becomes less apparent in its southern coastal area. In the case of three clusters ($N_c = 3$), the 170km-D appears to deepen within the suture zone and the southern NAC (Figure S10 in the Supplementary Material). However, in the $N_c = 4$ case, this deepened region is instead classified as part of the subsequent deeper interface at 220km depth (220km-D).

The deeper X-Ds (220km-D, 260km-D, 310km-D) are distributed across the entire continent, with generally flat lateral patterns at each reference depth (Figures 5 and 11 (c–h)). However, both the 270km-D and 310km-D exhibit gradual lateral variations. The 270km-D becomes shallower in eastern Australia and along the Proterozoic suture zone (250–260 km), whereas it reaches depths of about 275 km beneath the southern part of NAC, the Albany-Fraser belt, and across the SAC (Figure 11 (e, f)). For the 310km-D, its depth appears to correlate with the distribution of cratonic blocks; it is relatively shallow (300 km) beneath the SAC, while it becomes deeper (320 km) beneath the WAC and NAC (Figure 11 (g, h)).

The depths of these X-Ds are consistent with previously detected interfaces. A recent S-wave receiver function study detected a positive S-wave speed jump around 150 km (Hua et al., 2023). In the continental region, the positive velocity gradient at 150 km (PVG-150) would be concentrated primarily in the Phanerozoic and younger orogenic zones, possibly consistent with our 170km-D. In addition, they noted a globally sporadic positive velocity gradient at 260 km (PVG-260), consistent with our 270km-D. Classical seismic studies also reported multiple upper mantle discontinuities with positive velocity jumps from 200 to 350 km under the LAB (Hales et al., 1980; Drummond et al., 1982; Leven, 1985; Revenaugh and Jordan, 1991), which generally corroborate our results.

4.4. Mid-lithospheric discontinuities

Our results indicate the presence of multiple MLDs (Figures 6, 7, and S6). Similar to the X-Ds, we applied the clustering analysis to the CPs of MLDs prior to mapping. In identifying MLDs, we considered S-velocity changes without distinguishing between positive and negative shifts. For clustering analysis, we included vertical changes in

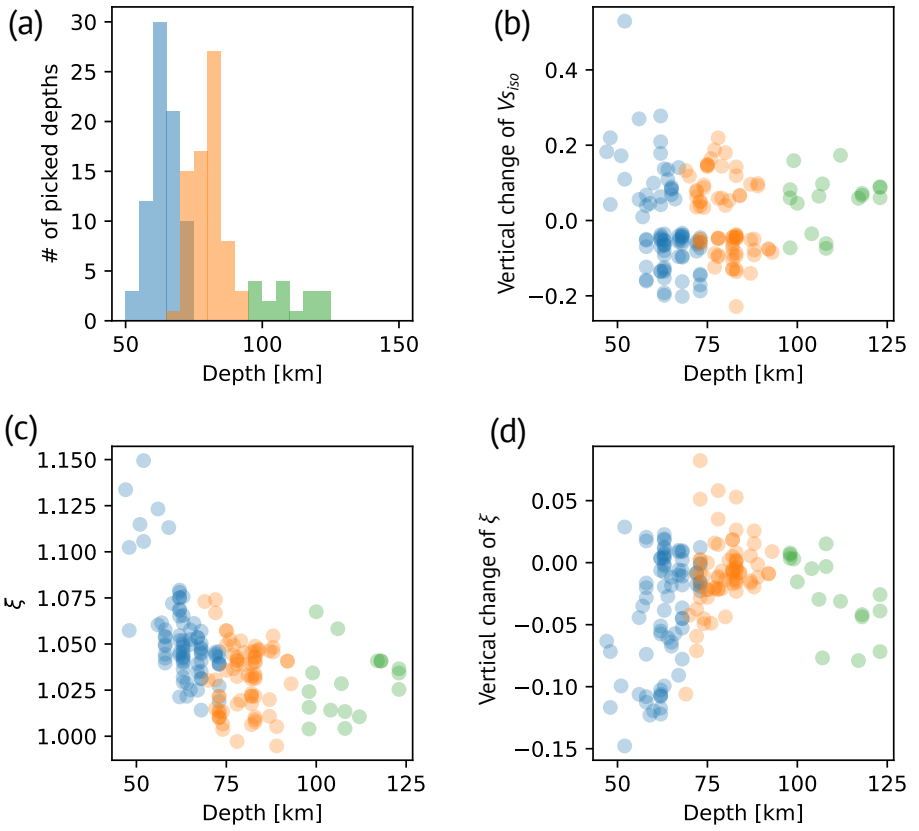


Figure 12: Same as Figure 10, but for MLDs.

S-wave speed among the five parameters used to classify the groups of X-Ds. Here, we set the number of clusters for MLDs to 3, as the $N_c = 4$ case lowered the silhouette score.

Figure 12 shows the results of clustering analysis for the CPs of MLDs. Depth is the primary parameter in this clustering, as with the X-Ds. We designate clusters 1 to 3 as MLD1, MLD2, and MLD3, respectively. Figure 13 provides three types of maps for each MLD: depth distribution (leftmost panels), the signs of vertical changes in S-wave speed and radial anisotropy (second and third panels), and the radial anisotropy (rightmost panel). Unlike other interfaces, we did not create interpolated maps of MLDs, as each MLD class contains both positive and negative velocity changes.

Our results reveal that MLDs comprise multiple interfaces at three depths: MLD1 at 60–70 km, MLD2 at 75–90 km, and MLD3 around 100 km (Figures 12 (a) and 13 (a-1, b-1, c-1)). Distinct MLDs are evident in the three cratonic blocks (WAC, SAC, NAC). MLD1 and MLD2 are present beneath all three cratonic blocks, whereas MLD3 is sparse in the WAC and SAC. In the suture zone, MLDs are mapped only in the Musgrave province and the Albany-Fraser belt (Figures 13 (a-1, b-1)). The depth distributions of MLD1 and MLD2 are consistent with previous S-RF observations (Ford et al., 2010; Birkey et al., 2021), which identified MLDs characterized by negative S-velocity changes. In this study, however, we observe both positive and negative S-velocity changes across MLDs (Figures 12 (b) and 13 (b-1, b-2,

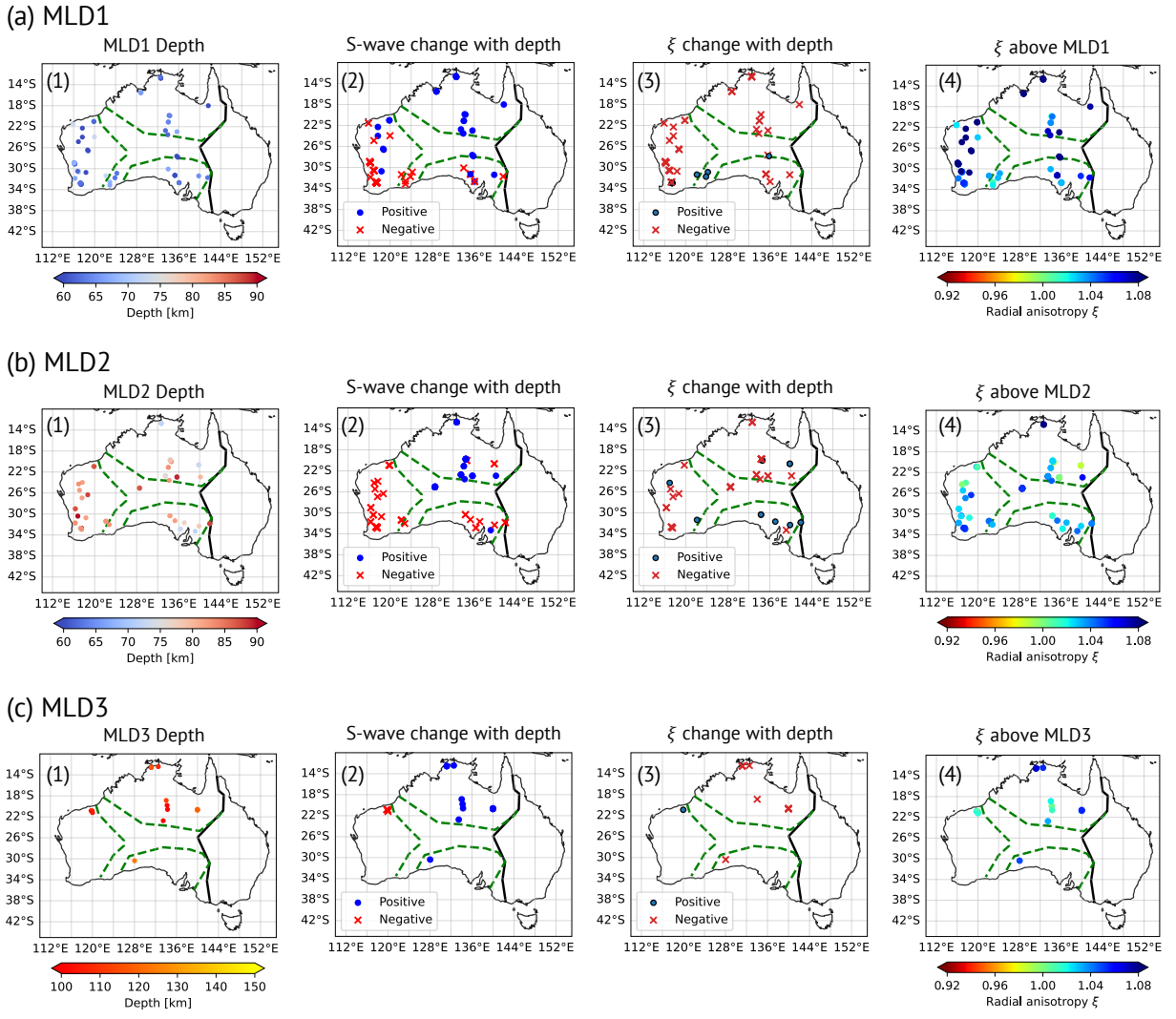


Figure 13: Spatial distribution of each MLD group: (a) MLD1 (blue in Figure 12), (b) MLD2 (orange in Figure 12), and (c) MLD3 (green in Figure 12). The left panels, (1), show the depth of MLD conversion points. The second and third panels, (2) and (3), display the vertical changes in isotropic S-wave speed and radial anisotropy, with circles and crosses indicating positive and negative changes, respectively. MLD CPs with smaller change in ξ (< 1 %) are excluded, so symbol locations may differ between the second and third panels. The right panels, (4), visualize the radial anisotropy above each MLD. Black solid and green dashed lines denote the Tasman Line and major tectonic boundaries of the WAC, NAC, and SAC, respectively.

c-1, c-2)). Additionally, the vertical variation in shear wave velocity (δV_S) and radial anisotropy ($\delta\xi$) across MLDs shows dependence on the tectonic province (two right panels in Figure 13 (a, b, c)). We will subsequently provide separate discussions for MLD1/MLD2 and MLD3.

In the WAC, excluding the Albany-Fraser belt (AF), we mainly observe two MLDs (MLD1 and MLD2). For MLD1, negative δV_S is concentrated along the continental margin, while positive δV_S is only found within the Archean (Pilbara and Yilgarn) cratons (Figure 13 (a-2, b-2)). In contrast, $\delta\xi$ in the WAC is generally negative, regardless of location

and depth. Around AF, δV_S is negative, as in the WAC, but this region shows positive $\delta\xi$ (Figure 13 (a-2, b-2)). In the SAC, δV_S is primarily negative, while $\delta\xi$ varies with depth: negative at MLD1 and positive at MLD2 (Figure 13 (a-2, b-2)). In most areas of the NAC, δV_S across MLD1 and MLD2 is generally positive, contrasting to earlier results from S-RFs studies (Ford et al., 2010; Birkey et al., 2021).

MLD3 (Figure 13 (c)) is largely absent in most cratonic regions except for the NAC, associated with positive δV_S at around 100 km. Outside the NAC, MLD3 appears only beneath the Pilbara craton (Archean) and the Coompuna province (Proterozoic) (Pi and Co in Figure 1), with negative $\delta\xi$ in the NAC and SAC, and positive in the Pilbara craton of the WAC.

MLD1 and MLD2 in the WAC and SAC generally show S-wave velocity reductions, consistent with earlier S-RF studies involving other continental regions (e.g, Abt et al., 2010; Kumar et al., 2012; Liu et al., 2020; Birkey et al., 2021). However, in the NAC, we find multiple MLDs characterized by distinct positive velocity jumps, agreeing with early observations of a positive step-like velocity jump in mid-lithospheric depths (∼75 km) (Hales et al., 1980; Leven, 1985). Similar observations of positive MLD velocity jumps have also been made in North America (Calò et al., 2016), including that MLDs are not exclusively associated with S-wave velocity reductions. Across MLDs, vertical changes in radial anisotropy are primarily negative (Figure 12), though some positive changes appear in MLD2 beneath the SAC (Figure 13 (b)). This continental-scale observation may provide new insights into the nature of seismological MLDs.

The rightmost panels in Figure 13 display radial anisotropy ξ above each MLD. Considering $\delta\xi$ (Figure 13 (a-3, b-3, c-3)), as well as Figure 12 (c), radial anisotropy generally decreases with depth, approaching isotropy. This trend, previously reported by Yoshizawa and Kennett (2015) and Kennett et al. (2017), is particularly evident in the WAC and NAC.

5. Discussion

5.1. Comparison with previous MLD distribution

We can find Ps conversion points at multiple depths in the cratonic lithosphere, which are characterized by not only $\delta V_S < 0$ but also $\delta V_S > 0$ in Figures 12 and 13. As explained in the previous section, the MLD beneath the NAC comprises multiple interfaces accompanied by $\delta V_S > 0$, contrasting to recent S-RF observations (Ford et al., 2010; Birkey et al., 2021). We will discuss the causes of positive interfaces and the discrepancies between S-RF observations in the next subsection. The MLDs characterized by $\delta V_S < 0$ from the earlier S-RF analysis (Ford et al., 2010; Birkey et al., 2021) are also detected in this study and widely distributed in the WAC and SAC (i.e., except for the NAC) below 75 km-depth (Figure 13). However, some MLD CPs in the WAC and SAC accompany the positive velocity gradient, mainly in the shallow depth above 70 km (Figure 13), which has not been reported in earlier S-RF studies in Australia (Ford et al., 2010; Birkey et al., 2021).

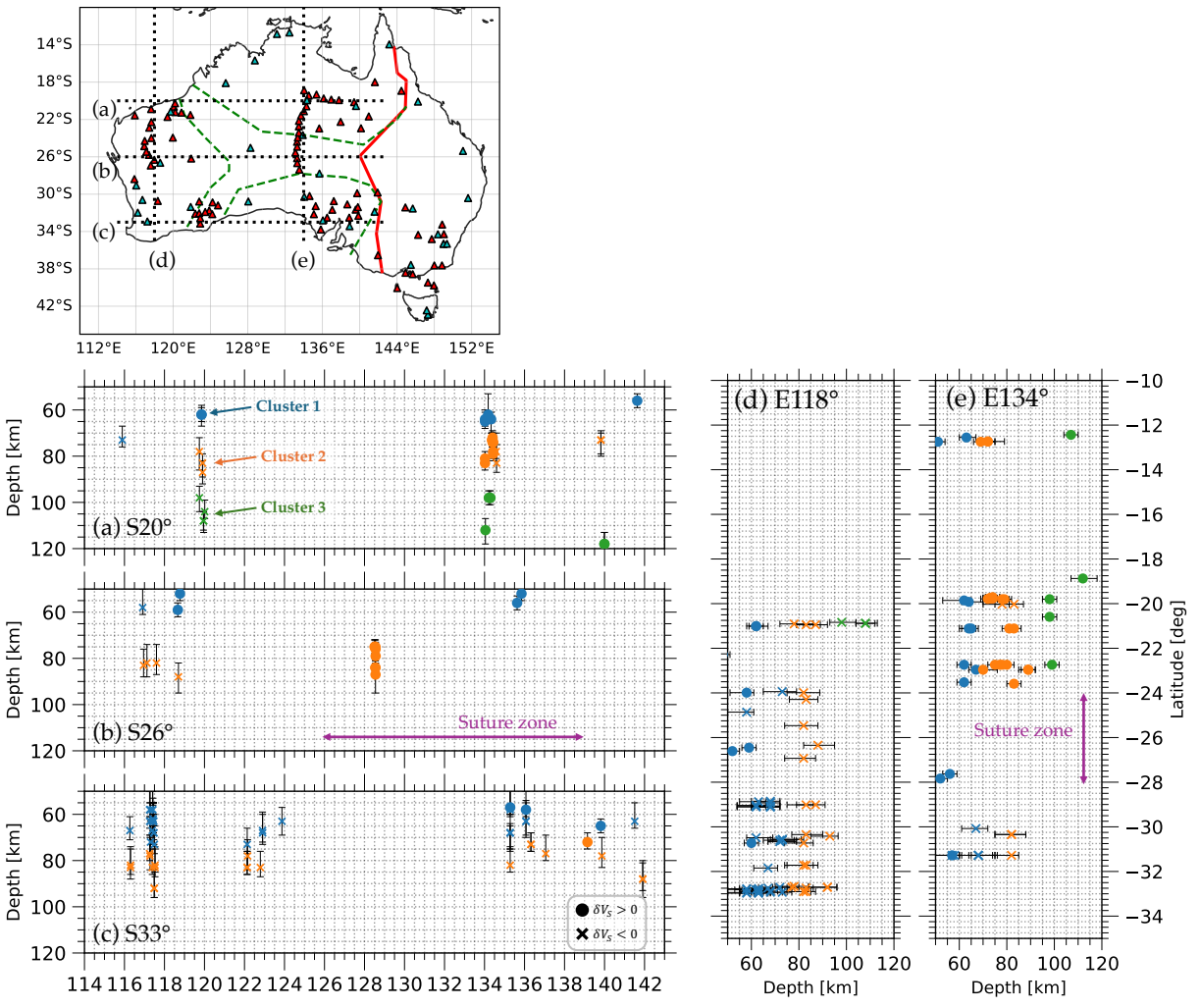


Figure 14: Cross-sectional view of clustered MLD conversion points. The top-left panel shows the station distribution used in this study (cyan: permanent stations, red: temporary stations), where the dashed lines labeled with (a–e) indicate the cross-sectional lines. (a–c) E-W cross-sectional plots of the MLD CPs. The selection criteria for CPs are the same as in Figure 5, but the background tomography models are excluded. The colored dots and crosses (blue: MLD1, orange: MLD2, green: MLD3) denote the MLD CPs corresponding to positive and negative δV_s, respectively. Error bars represent the IQR-based uncertainties, which are estimated from the inverted posterior distributions. The purple arrows indicate the lateral extent of the suture zone. (d, e) Same as (a–c), but for the N-S cross-sections.

Figure 14 illustrates the cross-sectional conversion points (CPs) of three MLDs classified in this study, representing the vertical distributions of CPs for multiple MLDs. While the MLDs associated with $\delta V_S > 0$ (positive MLD) exist at multiple depths in the NAC, they distributed mainly in the shallower MLD1 group in the WAC and SAC (Figure 14), especially beneath the Archean cratons of Pilbara, Yilgarn, and Gawler. In particular, the shallow positive MLD in the WAC cannot be observed at the continental margin and appears only within the Archean Yilgan and Pilbara cratons (Figure 13).

Birkey et al. (2021) employed S-RFs and detected negative MLDs in the cratonic region, though just a single MLD was found in the southern WAC. On the other hand, Sun et al. (2018) and Chen et al. (2021b) estimated multiple lithospheric discontinuities through P-wave reflectivities and harmonic decompositions of azimuth-dependent P-RFs, respectively. Our maps of MLDs shown in Figures 13 and 14 support the latter studies based on the teleseismic P-waves. Such differences in P and S-wave analysis results may be due to the intrinsic differences in the wavelength and conversion (or piercing) points of the incident P or S waves. The sensitive region of the S-to-p (Sp) converted phases of the S-RF tends to be much broader than that of P-to-s (Ps) phases; e.g., the conversion points are approximately 40–60 km away from the station for Ps and 100–150 km for Sp (for CPs at around 100 km depth). The P-wave-based analysis reflects the structure near the seismic station, which may better constrain multiple discontinuities under the station than S-RFs.

5.2. Interpretations of MLDs

The mid-lithospheric discontinuities (MLDs) beneath Archean and Proterozoic cratonic regions likely record ancient tectonic processes such as formation, deformation, and thermal events. Numerous studies have attempted to explain the origins of MLDs, often characterized by negative velocity contrasts at lithospheric depths. These explanations, derived from seismological and petrological observations, laboratory experiments, and geodynamic modeling in the mantle, remain debated (e.g., Karato et al., 2015; Selway et al., 2015; Yoshizawa and Kennett, 2015; Chen et al., 2021b; Fu et al., 2022; Birkey and Ford, 2023; Sudholz et al., 2024). Proposed causes of MLDs include thermal effects (e.g., Karato et al., 2015), chemical compositional changes (e.g., Selway et al., 2015; Sudholz et al., 2024), and the layered anisotropy (e.g., Yoshizawa and Kennett, 2015; Ford et al., 2016; Birkey and Ford, 2023). While this study focuses on thermal and anisotropic properties, chemical layering may also contribute to MLD formation, reflecting the complexity of cratonic evolution, though unconstrained by our seismological data.

In the following, we discuss the causes of MLDs by investigating the sign of δV_S, incorporating information on radial anisotropy and our lithospheric thickness model (Figure 9).

5.2.1. MLDs accompanying S-velocity reduction ($\delta V_S < 0$)

MLDs characterized by S-wave velocity reductions ($\delta V_S < 0$) are observed at the edges of the Archean cratons in the WAC (Figure 13 (a-2, b-2)). At these depths, radial anisotropy is strong ($\approx$ 7–8 %) with $\delta\xi < 0$ (Figures 13 (a-3, 4, b-3, 4)), suggesting the presence of a cold, rigid craton that preserves the imprint of past tectonic processes. These MLDs are unlikely to be thermally induced, as the thermal effects would typically result in a more deformable lithosphere, as supported by temperature models (Tesauro et al., 2020). Recent seismological studies (Chen et al., 2021b,a; Birkey and Ford, 2023) suggest that the topography of the lithospheric base along the western margin of the WAC may be related to MLDs, as inferred from azimuth-dependent P-RFs and/or SKS splitting analyses. In particular,

Birkey and Ford (2023) suggested that lithosphere thinning to the west of the western WAC margin could promote the edge-driven mantle convection, which is consistent with features in our LAB map (Figure 9).

The Albany-Fraser orogeny belt (AF), adjacent to the Yilgarn craton, also exhibits MLDs with negative δV_S, and an increase in radial anisotropy ($\delta\xi > 0$) across the MLD (Figure 13 (a-2, 3 and b-2, 3)). Strong radial anisotropy ($\approx$ 5–6 %) at lithospheric depths (Figure 13 (a, b, c-4)and the earlier tomographic model by Yoshizawa (2014)) likely reflects the influence of mid-Proterozoic orogenic events at ~1300 Ma and 1160 Ma (Clark et al., 2000; Spaggiari et al., 2015). Rapid post-orogenic cooling, particularly in the western AF region (Scibiorski et al., 2015, 2016), may have contributed to localized lithospheric thickening (Figure 9).

In the eastern part of SAC, multiple MLDs with $\delta V_S < 0$ are observed, but the associated changes in $\delta\xi$ differ between MLD1 and MLD2. The shallower MLD shows characteristics similar to those in the WAC, with δV_S <0 and $\delta\xi < 0$, while the deeper MLD exhibits $\delta\xi > 0$, suggesting a more deformable deeper lithosphere. Yoshizawa (2014) attributed the thinner lithosphere beneath the Gawler craton to basal erosion associated with the rifting from the Antarctic continent. The presence of MLD2 may reflect remnants of this erosional process, potentially influenced by hot asthenospheric material, as indicated by elevated temperatures beneath the SAC (McLaren et al., 2003; Goes et al., 2005; Tesauro et al., 2020).

5.2.2. MLDs accompanying S-velocity increase $\delta V_S > 0$

MLDs in the NAC and at shallow depths beneath the Archean cratons in the WAC are identified by positive S-wave velocity gradients ($\delta V_S > 0$; middle panels in Figure 13). Unlike MLDs characterized by negative gradients ($\delta V_S < 0$), these features can be interpreted as step-like increase in S-wave velocity, likely resulting from surface cooling processes during the formation of stable continental lithosphere. Although our observations contrast with results from S-RF studies (e.g., Ford et al., 2010; Birkey et al., 2021) that indicate the negative velocity changes, they are consistent with earlier findings based on regional P-wave analyses (Hales et al., 1980; Leven, 1985).

A plausible explanation for these discrepancies can be the influence of complex anisotropic layering, in addition to the inherent differences between P- and S-RFs. Selway et al. (2015) demonstrated that both azimuthal and radial anisotropic layering can produce negative phases in S-RFs, complicating the interpretation of seismic discontinuities. Moreover, rapid vertical and lateral variations in lithospheric thickness, seismologically observed beneath northern and central Australia (Birkey and Ford, 2023; Yoshizawa, 2014; Yoshizawa and Kennett, 2015; de Laat et al., 2023), further increase the complexity of such interpretations. Reconciling S-RF results with our inversion-based P-RF results requires careful consideration of the influence of anisotropic structure on receiver functions (e.g. Park and Levin, 2016). In addition, fine-scale heterogeneities may induce apparent radial anisotropy and spurious seismic discontinuities (e.g., Fichtner et al., 2013; Kennett et al., 2017), further influencing RF observations.

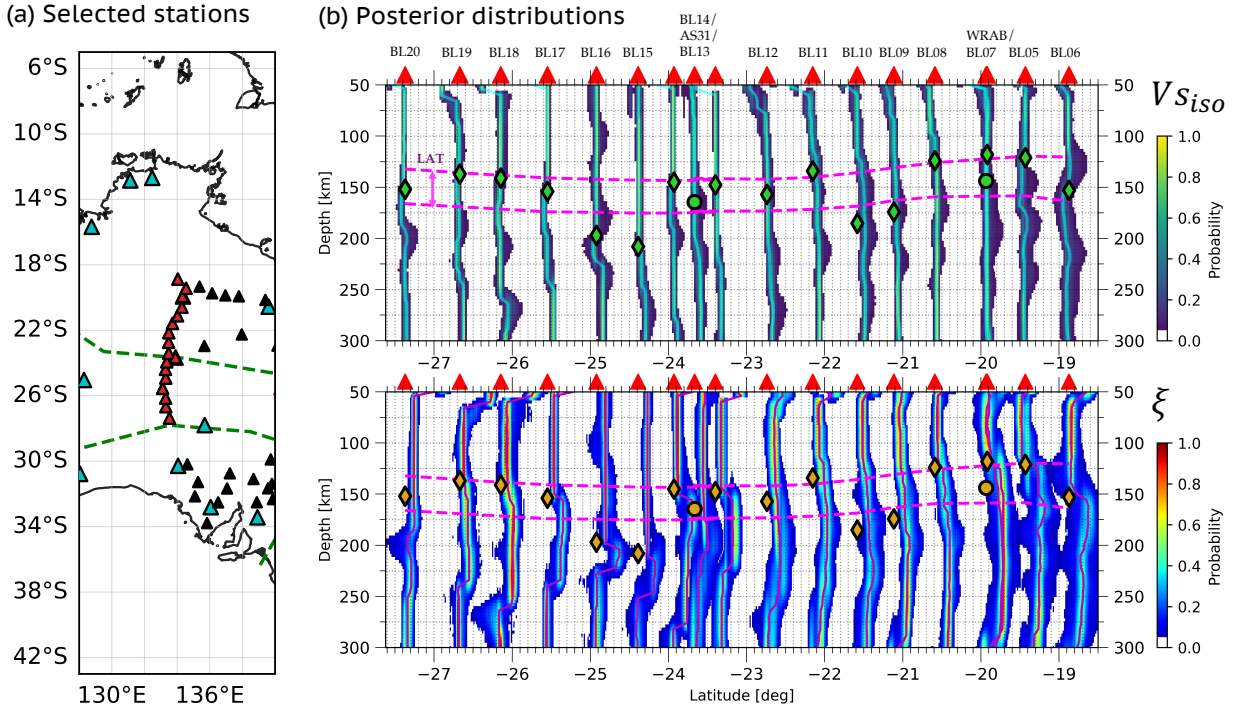


Figure 15: Posterior distributions of isotropic shear wave velocity and radial anisotropy at permanent and temporary stations deployed in central Australia. (a) Map of seismic stations. The red triangles represent the selected stations used in (b), while cyan and black ones correspond to other permanent and temporary stations. (b) Probabilistic profiles of isotropic S-wave (top panel) and radial anisotropy (bottom panel). In the top panel, the vertical profiles are plotted by adjusting the uppermost mantle S-velocity (or radial anisotropy) to be located at the latitude of stations. Colored dots and diamonds (green in the top panel and orange in the bottom panel) indicate the depths of the estimated lithospheric base for permanent stations (WRAB and AS31) and selected temporary stations (Rawlinson and Kennet, 2008), where the values for two permanent stations correspond to the azimuthally-averaged depths that are the same as in Figure 7. Colored lines (cyan in the top and magenta in the bottom) delineate the maximum frequency model derived from the ensemble solutions. Two pink curves exhibit the upper and lower bounds of the LAT from Yoshizawa (2014).

5.3. Thick lithosphere in central Australia

An anomalously thick lithosphere, reaching depths of about 200 km, is evident in the eastern Yilgarn craton, southern NAC, and the cratonic suture zone, as revealed by our joint inversion of receiver functions and multimode surface waves (Figure 9). In central Australia, significant radial anisotropy with weak S-wave velocity reduction is observed (Figures 7 (b, c), 15, and S6). This distinctive feature in the mid-Proterozoic province may reflect the ancient amalgamation processes during the mid-Proterozoic era (1300–1000 Ma) (Myers et al., 1996).

The Musgrave orogeny, located in the suture zone, experienced ultra-high temperatures around 1220-1120 Ma due to upwelling asthenospheric materials (Smithies et al., 2011, 2015), associated with the amalgamation of cratons. Such extreme thermal conditions could have weakened the lithospheric structure, enabling the suture zone to act as a buffer zone during the collision of the NAC, SAC, and WAC (e.g., Yoshida, 2012; Yoshida and Yoshizawa, 2020). Following this extensive tectonic-thermal event, central Australia, including the southern NAC, underwent repeated

deformation by compression and extension cycles until the Alice-Springs Orogeny (∼400 Ma) (Kennett and Iaffaldano, 2013; Thiel et al., 2020). These tectonic processes likely influenced both the lithosphere-asthenosphere system and the crustal structure beneath the region. Anomalous radial anisotropy within the shallow lithosphere likely reflects frozen anisotropy preserved from past deformation processes, whereas that in the asthenosphere or near the lithospheric base (Figure 7 (c)) is more plausibly attributed to present-day deformation associated with ongoing shear flow in the mantle beneath the fast-moving Australian plate (e.g., Debayle and Kennett, 2000; Yoshizawa and Kennett, 2015).

The minimal S-wave speed drop provides insights into the unique lithospheric structure of central Australia. There are few records of the tectonic activity following the Alice Springs Orogeny (ASO, ∼400 Ma), which marked the last major tectonic event in this region (e.g., Aitken and Betts, 2009; Aitken et al., 2009), aside from some localized faulting and/or thermal erosion (e.g., Sandiford et al., 2001). This implies that the region has likely remained tectonically quiescent, experiencing little to no significant deformation or thermal disturbance since the ASO. Such long-term tectonic stability may have allowed the lithosphere to cool efficiently, facilitating the formation of a high-shear-wave-speed shield and preventing chemical or thermal erosion.

The ultra-high temperatures sustained until ∼ 1000 Ma (Smithies et al., 2011) may have contributed to the chemical depletion of the lithospheric mantle. Geochemical studies have revealed mild depletion in the Musgrave Province (Zhao and McCulloch, 1993; Smits et al., 2014), suggesting a relatively higher degree of depletion compared to adjacent regions, such as the Arunta block. In addition, joint seismic and gravity analyses detected a weakly negative density anomaly at 80-200 km depth beneath the present-day Proterozoic lithosphere van Gerven et al. (2004), which may reflect deep chemical depletion. Such depleted, low-density mantle may result from the underplating of upwelling asthenospheric material and could have contributed to the formation of the tectosphere (Jordan, 1975, 1978, 1988), consistent with the observed thick lithosphere with limited S-wave speed reductions.

The observed characteristics of MLDs at 60–130 km depth in the southern NAC, marked by a positive V_S contrast ($\delta V_S > 0$) and a decrease in radial anisotropy ($\delta\xi < 0$), potentially reflect a highly rigid and non-deformable lithospheric structure, supporting the hypothesis of prolonged the tectonic quiescence and stable lithospheric evolution in this region.

5.4. Origins of X-Ds

The resultant X-D maps reveal the existence of multiple interfaces below the lithospheric base, located at around 170 km, 220–270 km, and around 310 km depth (Figures 10 (a), 11, S9, and S10). Similar features have been reported in previous studies; for example, the NAC was suggested to host multiple velocity-increasing interfaces at around 200 km and 325 km (Hales et al., 1980; Leven, 1985), while the northwestern part of WAC was inferred to contain at least one interface near 200 km. Our results broadly support these earlier findings, despite limited evidence for such features

in the western WAC. Additionally, Revenaugh and Jordan (1991) and Taira and Yoshizawa (2020) inferred the presence of discontinuities with increasing velocity at depths between 180 and 340 km beneath the Australian continent, with depth variations depending on tectonic provinces. The X-Ds identified in this study (Figures 5 and 10) approximately coincide with the depths of these previously reported interfaces.

Figures S13–16 visualize the downward variations of isotropic S-wave velocity and radial anisotropy across each X-D, as well as the absolute value of the anisotropic parameter below the X-D. These X-Ds are characterized not only by S-wave speed increases but also by a weakening of radial anisotropy across the interfaces (Figures 5, 6, 7, S6, S7, and 10, S13–16), consistent with the previous findings on deeper discontinuities (Gaherty and Jordan, 1995; Taira and Yoshizawa, 2020). Such seismological evidence provides important clues to the enigmatic nature of these structures. In this subsection, we explore potential geophysical origins and roles of these X-Ds, with particular attention to their relationship with the Lehmann discontinuity.

5.4.1. 170km-discontinuity

The distribution of 170km-D, except for the NAC and the suture zone, appears robust under both the three- and four-cluster scenarios (Figures 11 and S10). The 170km-D is mainly observed in regions with relatively thin lithosphere, such as the Phanerozoic provinces and the eastern SAC, which correlate with high-temperature zones (Goes et al., 2005; Tesauro et al., 2020). This suggests that the thermal structure may play a key role in the formation of the 170km-D.

A global S-RF study by Hua et al. (2023) identified an interface with a positive velocity gradient at ∼150–180 km depth in young, tectonically active regions (e.g., eastern Australia), interpreted as the base of the low-velocity zone within the high-temperature asthenosphere. Our 1-D posterior density results for the eastern SAC and Phanerozoic Australia support this interpretation (Figures 6, 7, S6, and S7), as a pronounced low-velocity zone is clearly observed above the 170km-D. Thus, the 170km-D may represent the base of an anomalously low-velocity layer in the asthenospheric mantle.

Hua et al. (2023) proposed that the PVG-150 corresponds to the base of a partially molten layer, based on synthetic S-RF simulations. In easternmost Australia (e.g., G.CAN; AU.CNB; AU.YNG), our results indicate that the minimum isotropic S-wave velocity is about ∼4.4 km/s, which is generally higher than the expected threshold for partial melt ($V_{S_{iso}}$ <4.4 km/s, e.g., Hua et al. (2023)). Moreover, previous tomography studies (Fishwick et al., 2008; Yoshizawa, 2014; Magrini et al., 2023) have not identified such low-velocity zones beneath cratonic regions, including the SAC. Thus, the 170km-D found in this study likely represents the base of the low-velocity asthenosphere, without clear seismological evidence for partial melting. To further assess the role of partial melt in forming the 170km-D, further investigations should incorporate constraints from anelastic attenuation in the upper mantle (e.g. Dalton et al., 2008).

The 170km-D is also associated with a notable weakening in radial anisotropy, with a steeper decrease compared to other X-Ds (Figures 6, S6, S7, 10 (d), and S9 (d), S13 (b, e)). This trend is particularly evident in the southeastern Phanerozoic areas (Figures 6, S7, and S13 (b, e)), where anomalously high positive radial anisotropy above the discontinuity likely reflects intense asthenospheric flow (Figures 6, S6, and S7). Such a reduction in anisotropy may reflect a transition in mantle rheology from dislocation to diffusion creep, as demonstrated in laboratory experiments (Karato, 1992). This transition seismologically manifests as a shift from anisotropic to more isotropic properties, potentially making the base of the asthenosphere. In addition, mantle flow modeling by Eakin et al. (2023) suggests that strong asthenospheric flow occurs at depths of 120-150 km, gradually weakening toward 200 km. Thus, the rapid weakening in radial anisotropy across the 170km-D (Figures 6, S6, S7, and S13 (b, e)) likely reflects vertical variations in mantle flow strength, delineating the base of the ductile asthenosphere beneath the Phanerozoic province and eastern SAC.

5.4.2. Deeper X-discontinuities

The 220km-D, 270km-D and 310km-D are generally less distinct than the 170km-D, especially the shallower two among the three deeper X-Ds. For the $N_c = 3$ case in the clustering anlaysis, a portion of the 220km-D in the NAC and suture zone is assigned to cluster 1 (i.e., 170km-D), while the remainder of the 220km-D and the 270km-D appears to merge into a single deep interface at around 260 km (Figure 11 and S10).

These three deeper interfaces align with earlier findings from the body-wave-based type studies (Hales et al., 1980; Leven, 1985; Revenaugh and Jordan, 1991). As a hypothesis, the deeper X-Ds may correspond to mineral phase transitions. Previous studies on X-Ds below 200 km (e.g., Revenaugh and Jordan, 1991; Williams and Revenaugh, 2005; Kemp et al., 2019; Srinu et al., 2021; Pugh et al., 2023) suggest that the 220-280 km discontinuities may be associated with the phase transition from orthopyroxene (Opx) to high-pressure clinopyroxene (HPCpx) (Akashi et al., 2009; Jacobsen et al., 2010), characterized by positive Clapeyron slopes ($dP/dT > 0$). The depth correspondence between these phase transitions and the observed X-Ds is plausible: the 220km-D and 270km-D are consistent with the Opx-HPCpx transition depths under wet (Jacobsen et al., 2010) and dry (Akashi et al., 2009) conditions, respectively, whereas such correspondence is less clear for the 310km-D. Thus, the shallower two of the three deeper X-Ds may be explained by the Opx-HPCpx phase transition. However, significant lateral heterogeneity in both thermal and seismic structures across the Australian continent (e.g., Goes et al., 2005; Fishwick et al., 2008; Yoshizawa, 2014; Tesauro et al., 2020) may cause regional variations in phase transition depths, making robust interpretation of the 220km-D and 270km-D more challenging compared to the 170km-D.

A plausible explanation for 310km-D is that it marks the base of the anisotropic layer that defines the asthenosphere under stable continental areas. Above the 310km-D, the cratonic provinces, particularly the NAC and suture zone,

exhibit strong radial anisotropy, reflecting the horizontal shear-flow in the asthenosphere (Figures7 (b, c), S6, 15 and Yoshizawa (2014)). Approaching the 310km-D, radial anisotropy rapidly weakens in the western NAC, the suture zone, and the northern WAC (Figures 15, S6, S7, and S16 (b, e)), although the degree of change varies spatially. A similar trend is also observed across the 170km-D (Figure 6 and S13 (b, e)) under the Phanerozoic Australia, suggesting that the 310km-D may represent a deeper mechanical boundary under the cratonic areas caused by a rheological transition in mantle creep-behaviour (Karato, 1992). It may therefore mark the base of the asthenosphere beneath the cratonic regions.

5.4.3. Relationship with the Lehmann discontinuity

One or more of the detected X-Ds may correspond to the Lehmann discontinuity (L-D), first identified beneath continental regions by Lehmann (1961). The L-D has been attributed to a transition in mineral creep behavior from dislocation to diffusion (Karato, 1992), which seismologically manifests as a shift from anisotropic to more isotropic properties. Such a tendency is observed at the 170km-D beneath the Phanerozoic province and eastern SAC, and at the 310km-D beneath much of the cratonic region, both potentially representing the base of the ductile asthenosphere. Gaherty and Jordan (1995) and Taira and Yoshizawa (2020) suggested that the L-D may be associated with a reduction in radial anisotropy, which is consistent with our observations of X-Ds exhibiting decreasing anisotropy (Figures 5 and 10). Thus, it is plausible that one or more of the X-Ds identified in this study may correspond to the L-D, providing seismological interpretation for this enigmatic mantle discontinuity.

6. Conclusions

In this study, we conducted a comprehensive spatial mapping of the Australian upper mantle discontinuities using station-based 1-D S-velocity profiles derived from the joint Bayesian inversions of multimode surface waves and P-wave receiver functions. The results provide new seismological insights into the lithospheric and asthenospheric structure, advancing our understanding of the tectonic evolution of the continent. The key findings for each upper mantle interface are summarized as follows:

1. *Mid-Lithospheric Discontinuities (MLD):* Australian MLDs are found at multiple depths ranging from 60 to 120 km. Their elastic properties (S-velocity change, radial anisotropy) vary with tectonic provinces and depths, offering insights into their origins and relationships with ancient tectonic processes. The S-velocity changes across the MLDs depend on locations, with the velocity increase beneath the North Australian craton (NAC) and the velocity reductions in the West and South Australian Cratons (WAC and SAC)
2. *Lithospheric Thickness:* The lithospheric thickness exhibits significant regional variation across the Australian continent: 70–100 km in eastern Australia, 120–150 km in the cratonic blocks, 170–200 km in the suture zone

and the southern NAC. In these thicker lithospheric regions, anomalously strong radial anisotropy (≈ 10 %) is observed without significant S-wave speed reductions, potentially formed through the underplating of chemically depleted mantle during high-temperature conditions associated with the continental amalgamation in the mid-Proterozoic.

3. *X-discontinuities (X-Ds):* The X-Ds include multiple interfaces at depths around 170 km, 220–270 km, and around 310 km, forming three or four distinct groups. The 170km-D is observed primarily in the eastern young orogenic zone and the eastern SAC, which can be related to the thermal structure. A common feature of X-Ds is the increasing S-velocity with the weakening of radial anisotropy across these interfaces.

Acknowledgments

All seismograms used in this study were downloaded from the IRIS Data Management Center (https://ds.iris.edu/ds/nodes/dm
This study was partly supported by JST SPRING grant number JPMJSP2119 to KT and JSPS KAKENHI (grant number 24KJ0294 to KT; 20K04096 and 23K03539 to KY). We used ObsPy (Beyreuther et al., 2010) for downloading and analyzing all seismic waveform data, and generated all figures with matplotlib (Hunter, 2007), cartopy (Office, 2010), Generic Mapping Tools (Wessel et al., 2019), and PyGMT (Uieda et al., 2021). We are grateful to Toru Taira for sharing his original trans-dimensional Bayesian inversion codes, which were helpful in the development of this study. This study was partly conducted using the supercomputer system at the Information Initiative Center, Hokkaido University.

Data Availability

All seismograms used in this study are available from the IRIS Data Management Center (https://ds.iris.edu/ds/nodes/dmc/).

CRediT authorship contribution statement

Kotaro Tarumi: Conceptualization, Data curation, Methodology, Formal analysis, Funding acquisition, Investigation, Visualization, Software, Writing - Original draft. **Kazunori Yoshizawa:** Conceptualization, Data curation, Methodology, Funding acquisition, Investigation, Supervision, Writing – review and editing.

References

Abt, D.L., Fischer, K.M., French, S.W., Ford, H.A., Yuan, H., Romanowicz, B., 2010. North American lithospheric discontinuity structure imaged by Ps and Sp receiver functions. Journal of Geophysical Research: Solid Earth (1978–2012) 115. doi:10.1029/2009jb006914.

Aitken, A.R.A., Betts, P.G., 2009. Constraints on the Proterozoic supercontinent cycle from the structural evolution of the south-central Musgrave Province, central Australia. Precambrian Research 168, 284–300. doi:10.1016/j.precamres.2008.10.006.

Aitken, A.R.A., Betts, P.G., Weinberg, R.F., Gray, D., 2009. Constrained potential field modeling of the crustal architecture of the Musgrave Province in central Australia: Evidence for lithospheric strengthening due to crust-mantle boundary uplift. Journal of Geophysical Research: Solid Earth 114. doi:10.1029/2008jb006194.

Akashi, A., Nishihara, Y., Takahashi, E., Nakajima, Y., Tange, Y., Funakoshi, K., 2009. Orthoenstatite/clinoenstatite phase transformation in MgSiO3 at high-pressure and high-temperature determined by in situ X-ray diffraction: Implications for nature of the X discontinuity. Journal of Geophysical Research: Solid Earth 114. doi:10.1029/2008jb005894.

Akuhara, T., Yamashita, Y., Ohyanagi, S., Sawaki, Y., Yamada, T., Shinohara, M., 2023. Shallow Low-Velocity Layer in the Hyuga-Nada Accretionary Prism and Its Hydrological Implications: Insights From a Passive Seismic Array. Journal of Geophysical Research: Solid Earth 128. doi:10.1029/2022jb026298.

Beyreuther, M., Barsch, R., Krischer, L., Megies, T., Behr, Y., Wassermann, J., 2010. ObsPy: A Python Toolbox for Seismology. Seismological Research Letters 81, 530–533. doi:10.1785/gssrl.81.3.530.

Birkey, A., Ford, H.A., 2023. Anisotropic structure of the Australian continent. Frontiers in Earth Science 10, 1055480. doi:10.3389/feart.2022.1055480.

Birkey, A., Ford, H.A., Dabney, P., Goldhagen, G., 2021. The Lithospheric Architecture of Australia From Seismic Receiver Functions. Journal of Geophysical Research: Solid Earth 126. doi:10.1029/2020jb020999.

Bodin, T., Sambridge, M., Tkalčić, H., Arroucau, P., Gallagher, K., Rawlinson, N., 2012. Transdimensional inversion of receiver functions and surface wave dispersion. Journal of Geophysical Research: Solid Earth (1978–2012) 117, n/a–n/a. doi:10.1029/2011jb008560.

Boyce, A., Bodin, T., Durand, S., Soergel, D., Debayle, E., 2024. Seismic Evidence for Craton Formation by Underplating and Development of the MLD. Geophysical Research Letters 51. doi:10.1029/2023gl106170.

Calò, M., Bodin, T., Romanowicz, B., 2016. Layered structure in the upper mantle across North America from joint inversion of long and short period seismic data. Earth and Planetary Science Letters 449, 164–175. doi:10.1016/j.epsl.2016.05.054.

Chen, X., Levin, V., Yuan, H., 2021a. Small Shear Wave Splitting Delays Suggest Weak Anisotropy in Cratonic Mantle Lithosphere. Geophysical Research Letters 48. doi:10.1029/2021gl093861.

Chen, X., Levin, V., Yuan, H., Klaser, M., Li, Y., 2021b. Seismic Anisotropic Layering in the Yilgarn and Superior Cratonic Lithosphere. Journal of Geophysical Research: Solid Earth 126. doi:10.1029/2020jb021575.

Clark, D., Hensen, B., Kinny, P., 2000. Geochronological constraints for a two-stage history of the Albany–Fraser Orogen, Western Australia. Precambrian Research 102, 155–183. doi:10.1016/s0301-9268(00)00063-2.

Dalton, C.A., Ekström, G., Dziewoński, A.M., 2008. The global attenuation structure of the upper mantle. Journal of Geophysical Research: Solid Earth (1978–2012) 113. doi:10.1029/2007jb005429.

Davies, D.R., Rawlinson, N., Iaffaldano, G., Campbell, I.H., 2015. Lithospheric controls on magma composition along Earth's longest continental hotspot track. Nature 525, 511–514. doi:10.1038/nature14903.

Debayle, E., Kennett, B.L.N., 2000. The Australian continental upper mantle: Structure and deformation inferred from surface waves. Journal of Geophysical Research: Solid Earth 105, 25423–25450. doi:10.1029/2000jb900212.

de Laat, J.I., Lebedev, S., Celli, N.L., Bonadio, R., Chagas de Melo, B., Rawlinson, N., 2023. Structure and evolution of the Australian plate and underlying upper mantle from waveform tomography with massive data sets. Geophysical Journal International 234, 153–189. doi:10.1093/gji/ggad062.

Drummond, B.J., Muirhead, K.J., Hales, A.L., 1982. Evidence for a seismic discontinuity near 200km depth under a continental margin. Geophysical Journal International 70, 67–77. doi:10.1111/j.1365-246x.1982.tb06392.x.

Eakin, C.M., Davies, D.R., Ghelichkhan, S., O'Donnell, J.P., Agrawal, S., 2023. The Influence of Lithospheric Thickness Variations Beneath Australia on Seismic Anisotropy and Mantle Flow. Geochemistry, Geophysics, Geosystems 24. doi:10.1029/2023gc011066.

Fichtner, A., Kennett, B.L.N., Trampert, J., 2013. Separating intrinsic and apparent anisotropy. Physics of the Earth and Planetary Interiors 219, 11–20. doi:10.1016/j.pepi.2013.03.006.

Fishwick, S., Heintz, M., Kennett, B.L.N., Reading, A.M., Yoshizawa, K., 2008. Steps in lithospheric thickness within eastern Australia, evidence from surface wave tomography. Tectonics 27, n/a–n/a. doi:10.1029/2007tc002116.

Fontaine, F., Kennet, B., 2007. SOC - Southern Craton. URL: https://www.fdsn.org/networks/detail/7K_2007/.

Ford, H.A., Fischer, K.M., Abt, D.L., Rychert, C.A., Elkins-Tanton, L.T., 2010. The lithosphere–asthenosphere boundary and cratonic lithospheric layering beneath Australia from Sp wave imaging. Earth and Planetary Science Letters 300, 299–310. doi:10.1016/j.epsl.2010.10.007.

Ford, H.A., Long, M.D., Wirth, E.A., 2016. Midlithospheric discontinuities and complex anisotropic layering in the mantle lithosphere beneath the Wyoming and Superior Provinces. Journal of Geophysical Research: Solid Earth 121, 6675–6697. doi:10.1002/2016jb012978.

Fu, H., Li, Z., Chen, L., 2022. Continental Mid-Lithosphere Discontinuity: A Water Collector During Craton Evolution. Geophysical Research Letters 49. doi:10.1029/2022gl101569.

Gaherty, J.B., Jordan, T.H., 1995. Lehmann Discontinuity as the Base of an Anisotropic Layer Beneath Continents. Science 268, 1468–1471. doi:10.1126/science.268.5216.1468.

van Gerven, L., Deschamps, F., Hilst, R.D.v.d., 2004. Geophysical evidence for chemical variations in the Australian Continental Mantle. Geophysical Research Letters 31. doi:10.1029/2004gl020307.

Goes, S., Simons, F.J., Yoshizawa, K., 2005. Seismic constraints on temperature of the Australian uppermost mantle. Earth and Planetary Science Letters 236, 227–237. doi:10.1016/j.epsl.2005.05.001.

Hales, A., Muirhead, K., Rynn, J., 1980. A compressional velocity distribution for the upper mantle. Tectonophysics 63, 309–348. doi:10.1016/0040-1951(80)90119-5.

Hasterok, D., Halpin, J.A., Collins, A.S., Hand, M., Kreemer, C., Gard, M.G., Glorie, S., 2022. New Maps of Global Geological Provinces and Tectonic Plates. Earth-Science Reviews 231, 104069. doi:10.1016/j.earscirev.2022.104069.

van der Hilst, R., Kennett, B., 1993. SKIPPY. URL: https://www.fdsn.org/networks/detail/7B_1993/.

Hua, J., Fischer, K.M., Becker, T.W., Gazel, E., Hirth, G., 2023. Asthenospheric low-velocity zone consistent with globally prevalent partial melting. Nature Geoscience 16, 175–181. doi:10.1038/s41561-022-01116-9.

Hunter, J.D., 2007. Matplotlib: A 2D Graphics Environment. Computing in Science & Engineering 9, 90–95. doi:10.1109/mcse.2007.55.

Isse, T., Kawakatsu, H., Yoshizawa, K., Takeo, A., Shiobara, H., Sugioka, H., Ito, A., Suetsugu, D., Reymond, D., 2019. Surface wave tomography for the Pacific Ocean incorporating seafloor seismic observations and plate thermal evolution. Earth and Planetary Science Letters 510, 116–130. doi:10.1016/j.epsl.2018.12.033.

Jacobsen, S.D., Liu, Z., Ballaran, T.B., Littlefield, E.F., Ehm, L., Hemley, R.J., 2010. Effect of H2O on upper mantle phase transitions in MgSiO3: Is the depth of the seismic X-discontinuity an indicator of mantle water content? Physics of the Earth and Planetary Interiors 183, 234–244. doi:10.1016/j.pepi.2010.06.015.

Jordan, T.H., 1975. The continental tectosphere. Reviews of Geophysics 13, 1–12. doi:10.1029/rg013i003p00001.

Jordan, T.H., 1978. Composition and development of the continental tectosphere. Nature 274, 544–548. doi:10.1038/274544a0.

Jordan, T.H., 1988. Structure and Formation of the Continental Tectosphere. Journal of Petrology Special_Volume, 11–37. doi:10.1093/petrology/special_volume.1.11.

Karato, S., 1992. On the Lehmann discontinuity. Geophysical Research Letters 19, 2255–2258. doi:10.1029/92gl02603.

Karato, S.i., Olugboji, T., Park, J., 2015. Mechanisms and geologic significance of the mid-lithosphere discontinuity in the continents. Nature Geoscience 8, 509–514. doi:10.1038/ngeo2462.

Kemp, M., Jenkins, J., Maclennan, J., Cottaar, S., 2019. X-discontinuity and transition zone structure beneath Hawaii suggests a heterogeneous plume. Earth and Planetary Science Letters 527, 115781. doi:10.1016/j.epsl.2019.115781.

Kennet, B., 2000. West Australian Cratons. URL: https://www.fdsn.org/networks/detail/7G_2000/.

Kennett, B., 2003. TASMAL. URL: https://www.fdsn.org/networks/detail/7I_2003/.

Kennett, B., Debayle, E., Gorbatov, A., 1999. QUOLL. URL: https://www.fdsn.org/networks/detail/7F_1999/.

Kennett, B., Iaffaldano, G., 2013. Role of lithosphere in intra-continental deformation: Central Australia. Gondwana Research 24, 958–968. doi:10.1016/j.gr.2012.10.010.

Kennett, B., Saygin, E., 2015. The nature of the Moho in Australia from reflection profiling: A review. GeoResJ 5, 74–91. doi:10.1016/j.grj.2015.02.001.

Kennett, B., Yoshizawa, K., Furumura, T., 2017. Interactions of multi-scale heterogeneity in the lithosphere: Australia. Tectonophysics 717, 193–213. URL: http://www.sciencedirect.com/science/article/pii/S0040195117302913, doi:10.1016/j.tecto.2017.07.009.

Kennett, B.L.N., 2015. Lithosphere–asthenosphere P-wave reflectivity across Australia. Earth and Planetary Science Letters 431, 225–235. doi:10.1016/j.epsl.2015.09.039.

Kennett, B.L.N., Fichtner, A., Fishwick, S., Yoshizawa, K., 2013. Australian Seismological Reference Model (AuSREM): mantle component. Geophysical Journal International 192, 871–887. doi:10.1093/gji/ggs065.

Kennett, B.L.N., Gorbatov, A., Yuan, H., Agrawal, S., Murdie, R., Doublier, M.P., Eakin, C.M., Miller, M.S., Zhao, L., Czarnota, K., O'Donnell, J.P., Dentith, M., Gessner, K., 2023. Refining the Moho across the Australian continent. Geophysical Journal International 233, 1863–1877. doi:10.1093/gji/ggad035.

Kennett, B.L.N., Sippl, C., 2018. Lithospheric discontinuities in Central Australia. Tectonophysics 744, 10–22. doi:10.1016/j.tecto.2018.06.008.

Kim, S., Dettmer, J., Rhie, J., Tkalčić, H., 2016. Highly efficient Bayesian joint inversion for receiver-based data and its application to lithospheric structure beneath the southern Korean Peninsula. Geophysical Journal International 206, 328–344. doi:10.1093/gji/ggw149.

Kind, R., Mooney, W.D., Yuan, X., 2020. New insights into the structural elements of the upper mantle beneath the contiguous United States from S-to-P converted seismic waves. Geophysical Journal International doi:10.1093/gji/ggaa203.

Kumar, P., Kind, R., Yuan, X., Mechie, J., 2012. USArray Receiver Function Images of the Lithosphere-Asthenosphere Boundary. Seismological Research Letters 83, 486–491. doi:10.1785/gssrl.83.3.486.

Lehmann, I., 1961. S and the Structure of the Upper Mantle. Geophysical Journal International 4, 124–138. doi:10.1111/j.1365-246x.1961.tb06808.x.

Leven, J., 1985. The application of synthetic seismograms to the interpretation of the upper mantle P-wave velocity structure in northern Australia. Physics of the Earth and Planetary Interiors 38, 9–27. doi:10.1016/0031-9201(85)90119-0.

Liu, L., Tong, S., Li, S., Qaysi, S., 2020. Sp Receiver-Function Images of African and Arabian Lithosphere: Survey of Newly Available Broadband Data. Seismological Research Letters 91, 1813–1819. doi:10.1785/0220190311.

Magrini, F., Kästle, E., Pilia, S., Rawlinson, N., Siena, L., 2023. A New Shear-Velocity Model of Continental Australia Based on Multi-Scale Surface-Wave Tomography. Journal of Geophysical Research: Solid Earth 128. doi:10.1029/2023jb026688.

McLaren, S., Sandiford, M., Hand, M., Neumann, N., Wyborn, L., Bastrakova, I., 2003. Evolution and Dynamics of the Australian Plate doi:10.1130/0-8137-2372-8.157.

Myers, J.S., Shaw, R.D., Tyler, I.M., 1996. Tectonic evolution of Proterozoic Australia. Tectonics 15, 1431–1446. doi:10.1029/96tc02356.

Office, M., 2010. Cartopy: a cartographic python library with a Matplotlib interface URL: https://scitools.org.uk/cartopy.

Park, J., Levin, V., 2016. Anisotropic shear zones revealed by backazimuthal harmonics of teleseismic receiver functions. Geophysical Journal International 207, 1216–1243. doi:10.1093/gji/ggw323.

Plomerová, J., Kouba, D., Babuška, V., 2002. Mapping the lithosphere–asthenosphere boundary through changes in surface-wave anisotropy. Tectonophysics 358, 175–185. doi:10.1016/s0040-1951(02)00423-7.

Pugh, S., Boyce, A., Bastow, I.D., Ebinger, C.J., Cottaar, S., 2023. Multigenetic Origin of the X-Discontinuity Below Continents: Insights From African Receiver Functions. Geochemistry, Geophysics, Geosystems 24. doi:10.1029/2022gc010782.

Rawlinson, S., Kennet, B., 2008. BILBY. URL: https://www.fdsn.org/networks/detail/6F_2008/.

Reading, A., Kennett, B., 2005. CAPRA - Linkage. URL: https://www.fdsn.org/networks/detail/7J_2005/.

Reading, A., Rawlinson, N., 2011. Bass Strait. URL: https://www.fdsn.org/networks/detail/1P_2011/.

Revenaugh, J., Jordan, T.H., 1991. Mantle layering from ScS reverberations: 3. The upper mantle. Journal of Geophysical Research: Solid Earth 96, 19781–19810. doi:10.1029/91jb01487.

Rychert, C.A., Shearer, P.M., 2009. A Global View of the Lithosphere-Asthenosphere Boundary. Science 324, 495–498. doi:10.1126/science.1169754.

Sambridge, M., 2014. A Parallel Tempering algorithm for probabilistic sampling and multimodal optimization. Geophysical Journal International 196, 357–374. doi:10.1093/gji/ggt342.

Sandiford, M., Hand, M., McLaren, S., 2001. Tectonic feedback, intraplate orogeny and the geochemical structure of the crust: a central Australian perspective. Geological Society, London, Special Publications 184, 195–218. doi:10.1144/gsl.sp.2001.184.01.10.

Scibiorski, E., Tohver, E., Jourdan, F., 2015. Rapid cooling and exhumation in the western part of the Mesoproterozoic Albany-Fraser Orogen, Western Australia. Precambrian Research 265, 232–248. doi:10.1016/j.precamres.2015.02.005.

Scibiorski, E., Tohver, E., Jourdan, F., Kirkland, C.L., Spaggiari, C., 2016. Cooling and exhumation along the curved Albany-Fraser orogen, Western Australia. Lithosphere 8, 551–563. doi:10.1130/l561.1.

Selway, K., Ford, H., Kelemen, P., 2015. The seismic mid-lithosphere discontinuity. Earth and Planetary Science Letters 414, 45–57. doi:10.1016/j.epsl.2014.12.029.

Simons, F.J., Hilst, R.D.V.D., Montagner, J., Zielhuis, A., 2002. Multimode Rayleigh wave inversion for heterogeneity and azimuthal anisotropy of the Australian upper mantle. Geophysical Journal International 151, 738–754. doi:10.1046/j.1365-246x.2002.01787.x.

Sippl, C., 2016. Moho geometry along a north–south passive seismic transect through Central Australia. Tectonophysics 676, 56–69. doi:10.1016/j.tecto.2016.03.031.

Sippl, C., Brisbout, L., Spaggiari, C., Gessner, K., Tkalčić, H., Kennett, B., Murdie, R., 2017. Crustal structure of a Proterozoic craton boundary: East Albany-Fraser Orogen, Western Australia, imaged with passive seismic and gravity anomaly data. Precambrian Research 296, 78–92. doi:10.1016/j.precamres.2017.04.041.

Smithies, R., Kirkland, C., Korhonen, F., Aitken, A., Howard, H., Maier, W., Wingate, M., Gromard, R.Q.d., Gessner, K., 2015. The Mesoproterozoic thermal evolution of the Musgrave Province in central Australia — Plume vs. the geological record. Gondwana Research 27, 1419–1429. doi:10.1016/j.gr.2013.12.014.

Smithies, R.H., Howard, H.M., Evins, P.M., Kirkland, C.L., Kelsey, D.E., Hand, M., Wingate, M.T.D., Collins, A.S., Belousova, E., 2011. High-Temperature Granite Magmatism, Crust–Mantle Interaction and the Mesoproterozoic Intracontinental Evolution of the Musgrave Province, Central Australia. Journal of Petrology 52, 931–958. doi:10.1093/petrology/egr010.

Smits, R., Collins, W., Hand, M., Dutch, R., Payne, J., 2014. A Proterozoic Wilson cycle identified by Hf isotopes in central Australia: Implications for the assembly of Proterozoic Australia and Rodinia. Geology 42, 231–234. doi:10.1130/g35112.1.

Spaggiari, C., Kirkland, C., Smithies, R., Wingate, M., Belousova, E., 2015. Transformation of an Archean craton margin during Proterozoic basin formation and magmatism: The Albany–Fraser Orogen, Western Australia. Precambrian Research 266, 440–466. doi:10.1016/j.precamres.2015.05.036.

Srinu, U., Kumar, P., Haldar, C., Kumar, M.R., Srinagesh, D., Illa, B., 2021. X-Discontinuity Beneath the Indian Shield—Evidence for Remnant Tethyan Oceanic Lithosphere in the Mantle. Journal of Geophysical Research: Solid Earth 126. doi:10.1029/2021jb021890.

Sudholz, Z.J., Zhang, P., Eakin, C.M., Yaxley, G.M., Jaques, A.L., Frigo, C., Czarnota, K., 2024. Ancient Craton-Wide Mid-Lithosphere Discontinuity Controlled by Pargasite Channels. Geophysical Research Letters 51. doi:10.1029/2024gl108433.

Sun, W., Fu, L., Saygin, E., Zhao, L., 2018. Insights Into Layering in the Cratonic Lithosphere Beneath Western Australia. Journal of Geophysical Research: Solid Earth 123, 1405–1418. doi:10.1002/2017jb014904.

Taira, T., Yoshizawa, K., 2020. Upper-mantle discontinuities beneath Australia from transdimensional Bayesian inversions using multimode surface waves and receiver functions. Geophysical Journal International 223, 2085–2100. URL: https://doi.org/10.1093/gji/ggaa442, doi:10.1093/gji/ggaa442.

Tarumi, K., Yoshizawa, K., 2025. Detecting rapid lateral changes of upper mantle discontinuities using azimuth-dependent P-wave receiver functions and multimode surface waves doi:10.31223/x5km7j.

Tesauro, M., Kaban, M.K., Aitken, A.R.A., 2020. Thermal and Compositional Anomalies of the Australian Upper Mantle From Seismic and Gravity Data. Geochemistry, Geophysics, Geosystems 21. doi:10.1029/2020gc009305.

Thiel, S., Goleby, B.R., Pawley, M.J., Heinson, G., 2020. AusLAMP 3D MT imaging of an intracontinental deformation zone, Musgrave Province, Central Australia. Earth, Planets and Space 72, 98. doi:10.1186/s40623-020-01223-0.

Tkalčić, H., Chen, Y., Liu, R., Zhibin, H., Sun, L., Chan, W., 2011. Multistep modelling of teleseismic receiver functions combined with constraints from seismic tomography: crustal structure beneath southeast China. Geophysical Journal International 187, 303–326. doi:10.1111/j.1365-246x.2011.05132.x.

Tkalčić, H., Kennett, B., Sippl, C., Spaggiari, C., Gessner, K., 2013. Albany-Fraser Experiment. URL: https://www.fdsn.org/networks/detail/1K_2013/.

Tkalčić, H., Pasyanos, M.E., Rodgers, A.J., Gök, R., Walter, W.R., Al-Amri, A., 2006. A multistep approach for joint modeling of surface wave dispersion and teleseismic receiver functions: Implications for lithospheric structure of the Arabian Peninsula: MULTISTEP MODELING OF ARABIAN LITHOSPHERE. Journal of Geophysical Research: Solid Earth 111, n/a–n/a. doi:10.1029/2005jb004130.

Uieda, L., Tian, D., Leong, W.J., Jones, M., Schlitzer, W., Toney, L., Grund, M., Yao, J., Magen, Y., Materna, K., Newton, T., Anant, A., Ziebarth, M., Wessel, P., Quinn, J., 2021. PyGMT: A Python interface for the Generic Mapping Tools URL: https://doi.org/10.5281/zenodo.5607255, doi:10.5281/zenodo.5607255. the development of PyGMT has been supported by NSF grants OCE-1558403 and EAR-1948603.

Wessel, P., Luis, J.F., Uieda, L., Scharroo, R., Wobbe, F., Smith, W.H.F., Tian, D., 2019. The Generic Mapping Tools Version 6. Geochemistry, Geophysics, Geosystems 20, 5556–5564. doi:10.1029/2019gc008515.

Williams, Q., Revenaugh, J., 2005. Ancient subduction, mantle eclogite, and the 300 km seismic discontinuity. Geology 33, 1. doi:10.1130/g20968.1.

Yoshida, M., 2012. Dynamic role of the rheological contrast between cratonic and oceanic lithospheres in the longevity of cratonic lithosphere: A three-dimensional numerical study. Tectonophysics 532, 156–166. doi:10.1016/j.tecto.2012.01.029.

Yoshida, M., Yoshizawa, K., 2020. Continental Drift with Deep Cratonic Roots. Annual Review of Earth and Planetary Sciences 49, 1–23. doi:10.1146/annurev-earth-091620-113028.

Yoshizawa, K., 2014. Radially anisotropic 3-D shear wave structure of the Australian lithosphere and asthenosphere from multi-mode surface waves. Physics of the Earth and Planetary Interiors 235, 33–48. doi:10.1016/j.pepi.2014.07.008.

Yoshizawa, K., Ekström, G., 2010. Automated multimode phase speed measurements for high-resolution regional-scale tomography: application to North America. Geophysical Journal International 183, 1538–1558. doi:10.1111/j.1365-246x.2010.04814.x.

Yoshizawa, K., Kennett, B.L.N., 2015. The lithosphere-asthenosphere transition and radial anisotropy beneath the Australian continent. Geophysical Research Letters 42, 3839–3846. doi:10.1002/2015gl063845.

Zhao, J.x., McCulloch, M.T., 1993. Melting of a subduction-modified continental lithospheric, mantle: Evidence from Late Proterozoic mafic dike swarms, in central Australia. Geology 21, 463–466. doi:10.1130/0091-7613(1993)021<0463:moasmc>2.3.co;2.

Supplementary material for "Mapping upper mantle discontinuities beneath the Australian continent using multimode surface waves and receiver functions"

K. Tarumi[1,2,*] and K. Yoshizawa[1,2]

[1] Department of Natural History Sciences, Graduate School of Science, Hokkaido University, Sapporo 060-0810, Japan

[2]Department of Earth & Planetary Sciences, Faculty of Science, Hokkaido University, Sapporo 060-0810, Japan.

[*]Corresponding author: tarumi.kotaro.jp@gmail.com

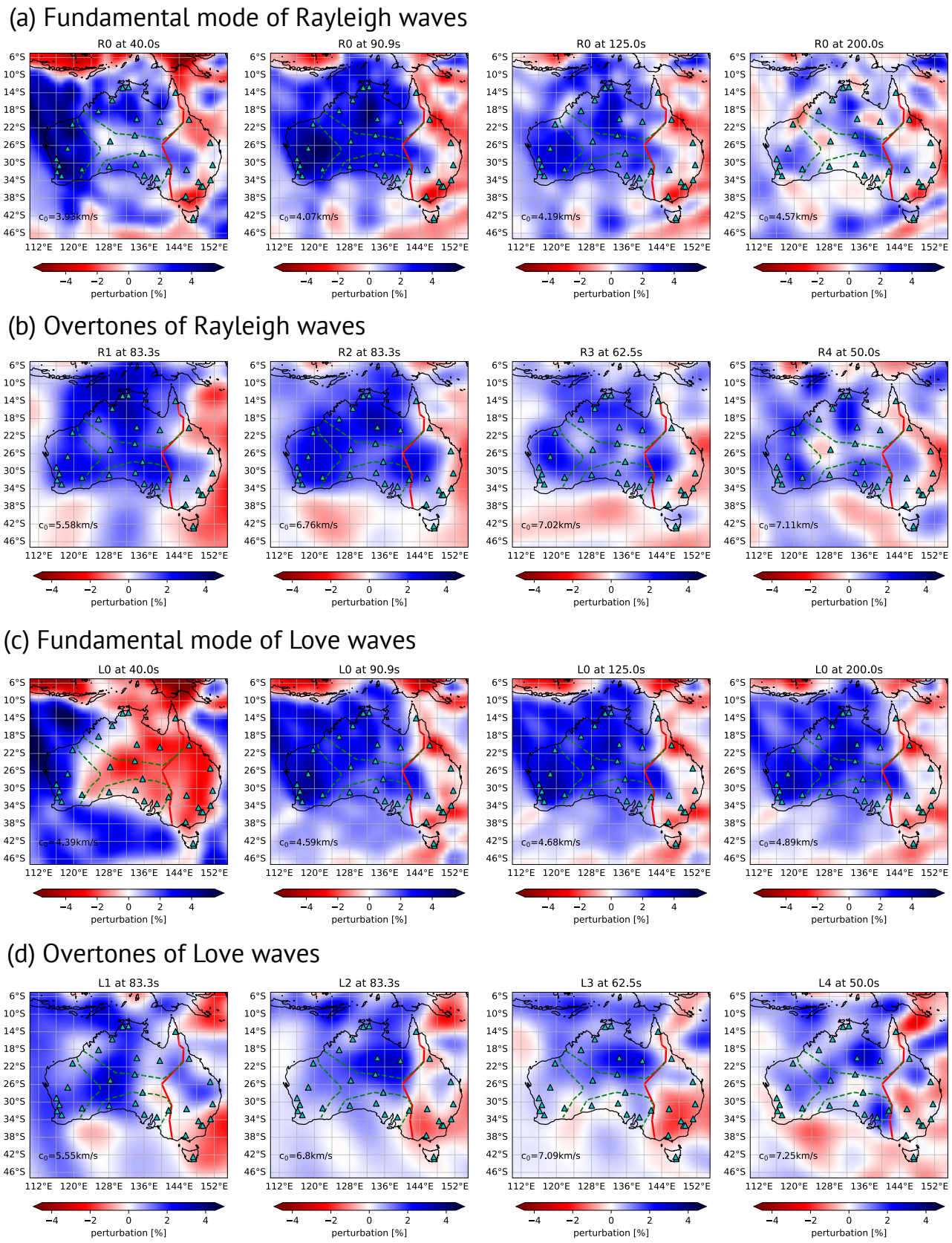


Figure S1: Multi-mode phase speed maps at selected periods from Yoshizawa (2014). R0

and L0 denote the fundamental modes of Rayleigh and Love waves, respectively, while higher modes (such as R2 and L4) indicate the overtones of Rayleigh and Love waves with mode numbers. Phase speed maps are shown as perturbations relative to a reference velocity, which is displayed at the bottom of each map. Cyan triangles denote locations of permanent seismic stations used in this study. Localized dispersion curves were extracted from these maps and employed as multimode dispersion data in the joint inversions with P-wave receiver functions.

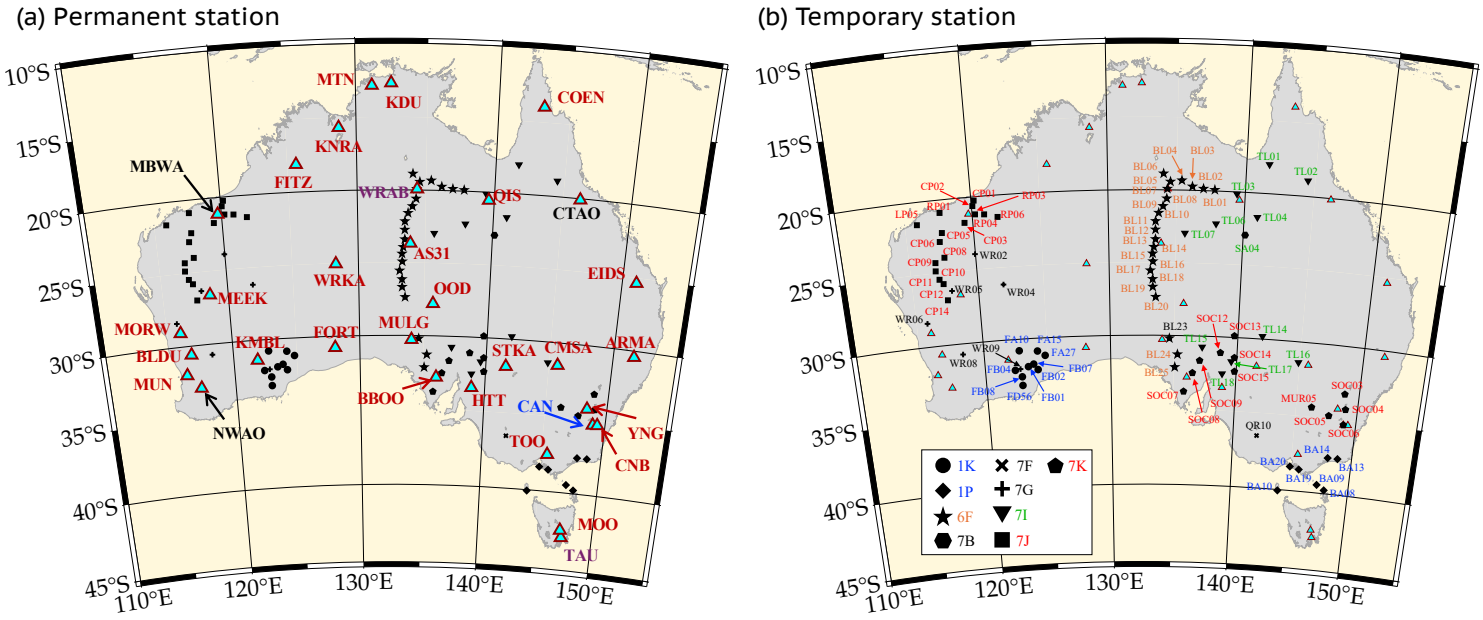


Figure S2: Distributions of all employed seismic stations. (a) Permanent stations (cyan triangles), labeled with station names. Font colors indicate seismic networks (IU: black; II: purple; G: blue; AU: red). Small black symbols represent temporary stations. (b) Same as (a), but showing the temporary stations with their names.

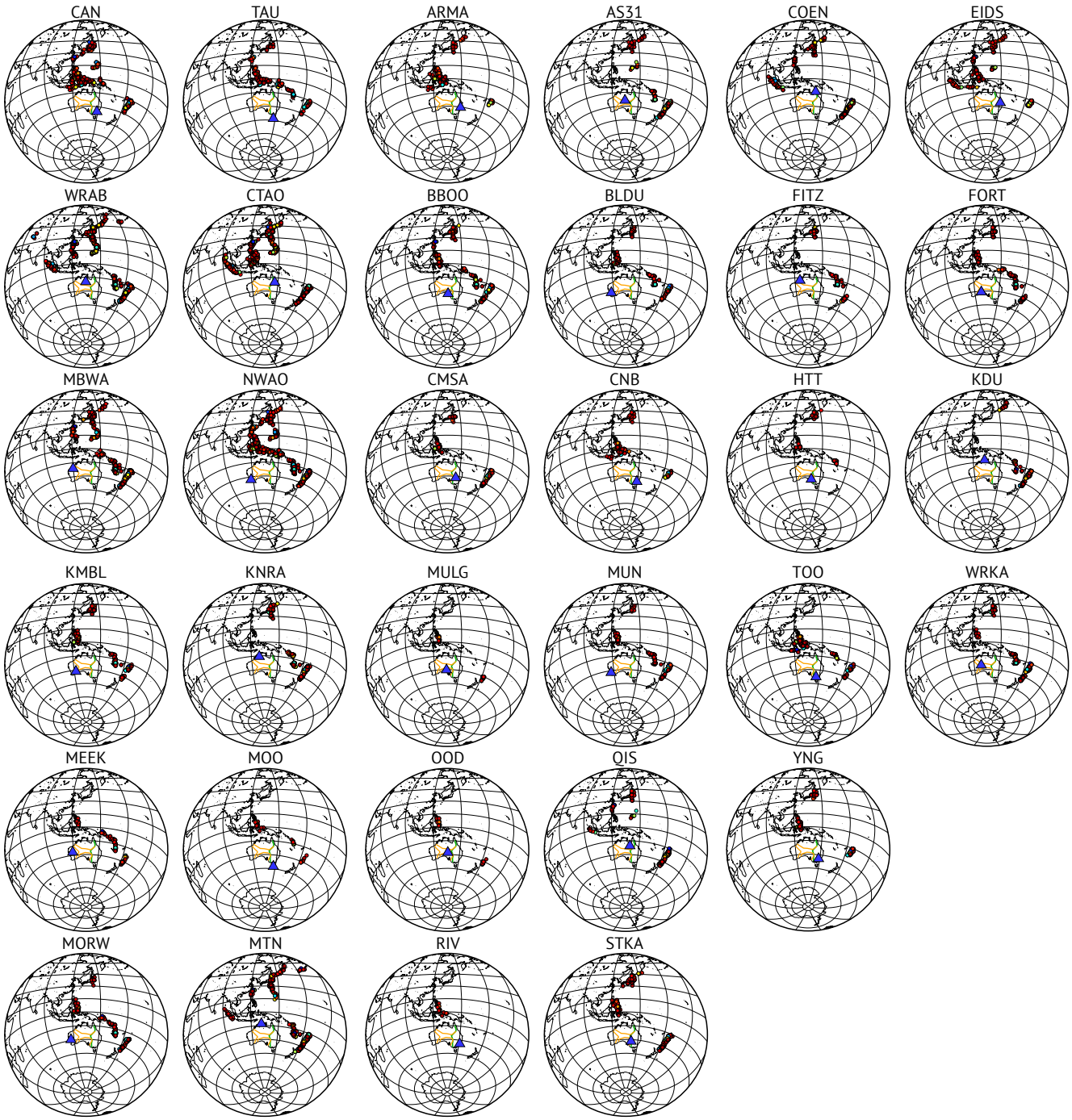


Figure S3: Event distributions for each station used in the receiver function analysis in this study.

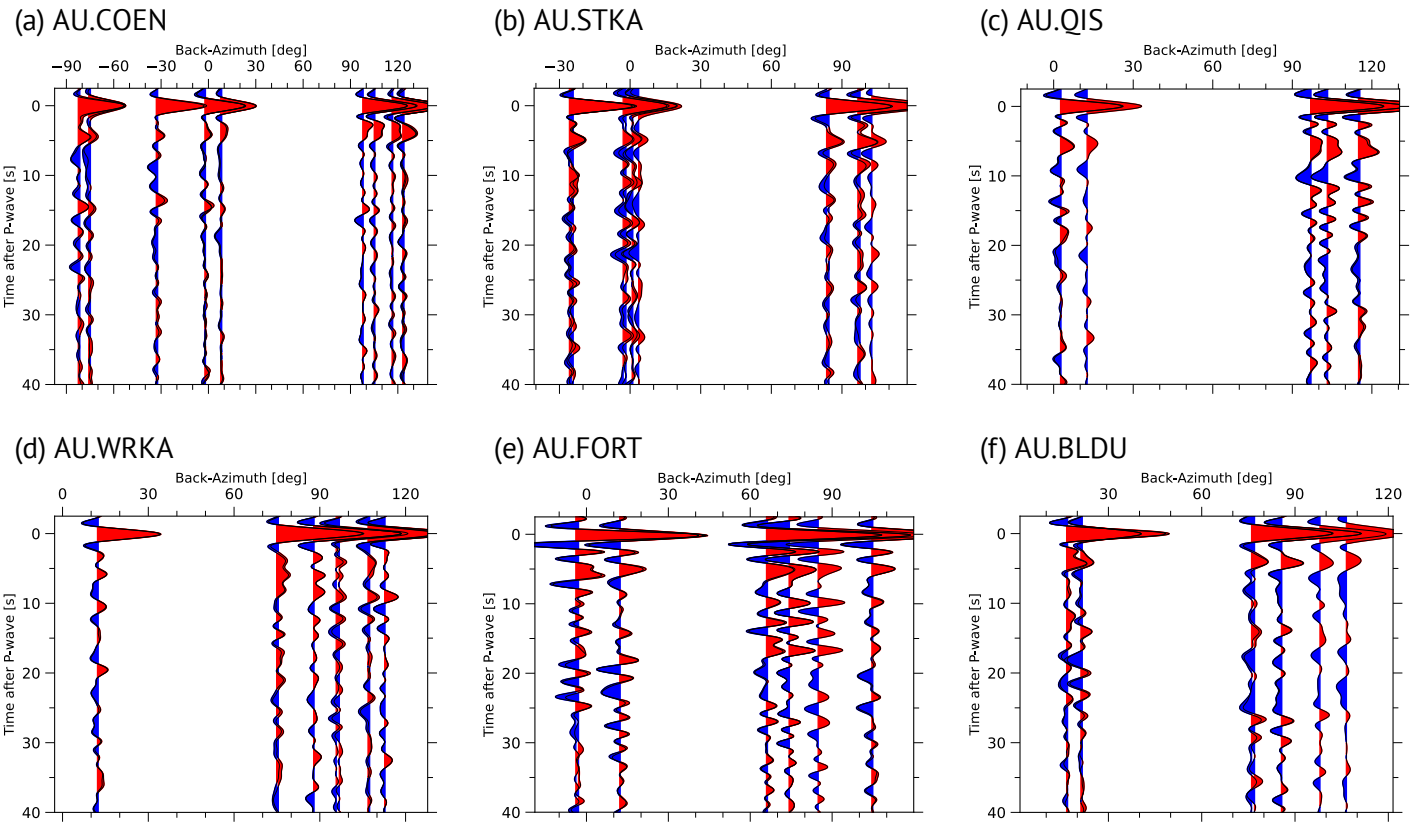


Figure S4: Same as Figure 3, but for 0.03-0.5 Hz.

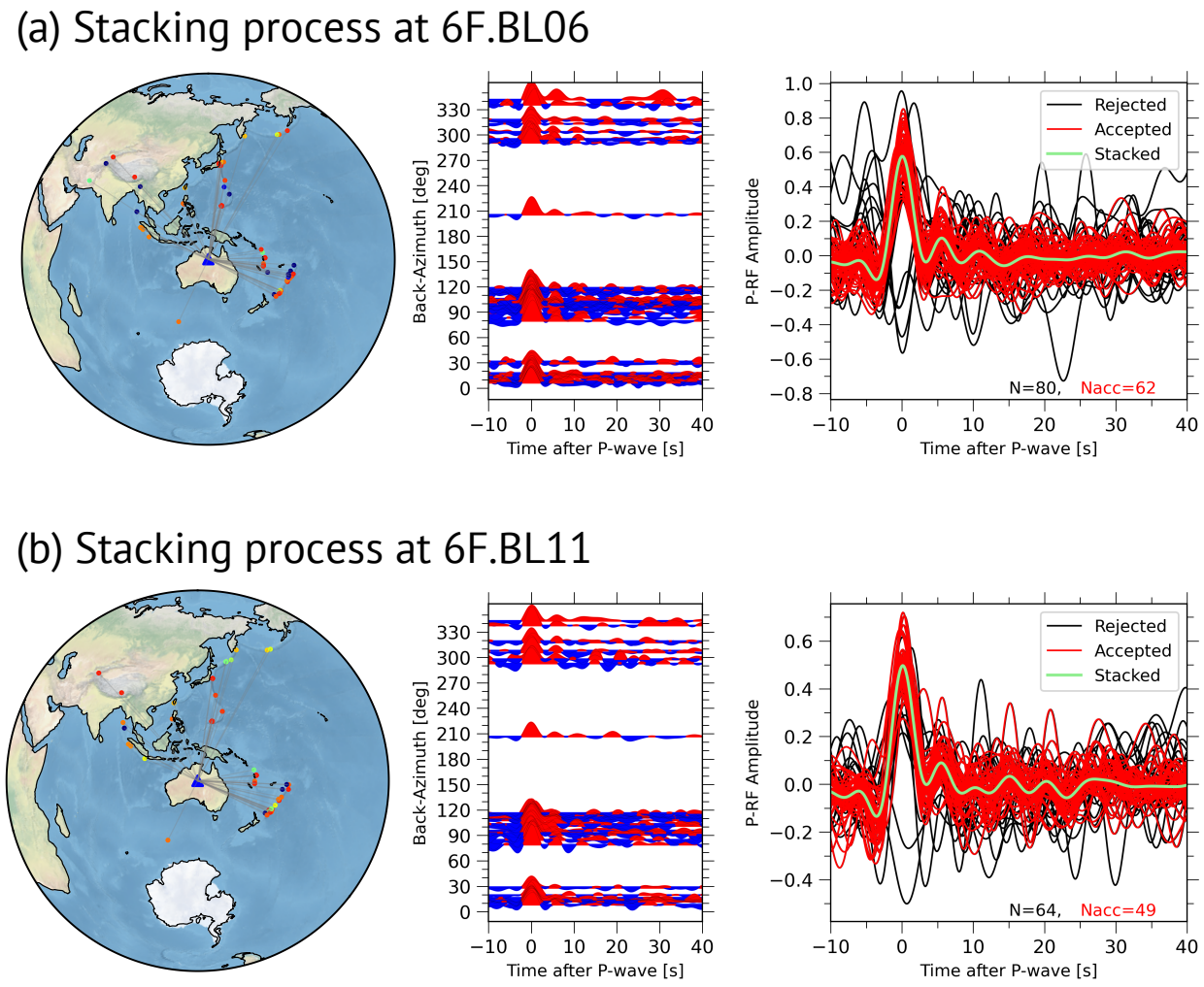


Figure S5: Examples of stacking processes for P-wave receiver functions (P-RFs) at two selected temporary stations: (a) 6F.BL06 and (b) 6F.BL11. (a) Stacking procedure for 6F.BL0. The leftmost panel shows the distribution of teleseismic events used for the P-RF analysis. The center panels show individual P-RF traces ordered by back azimuth, with positive and negative amplitudes shown in red and blue, respectively. The rightmost panel displays the stacking process for P-RF: black and red lines indicate traces rejected or accepted through the cross-correlation-based selection method (Tkalčić et al., 2011), while the light green line represents the final stacked trace used in our inversion analysis. (b) Same as (a), but for stations 6F.BL11.

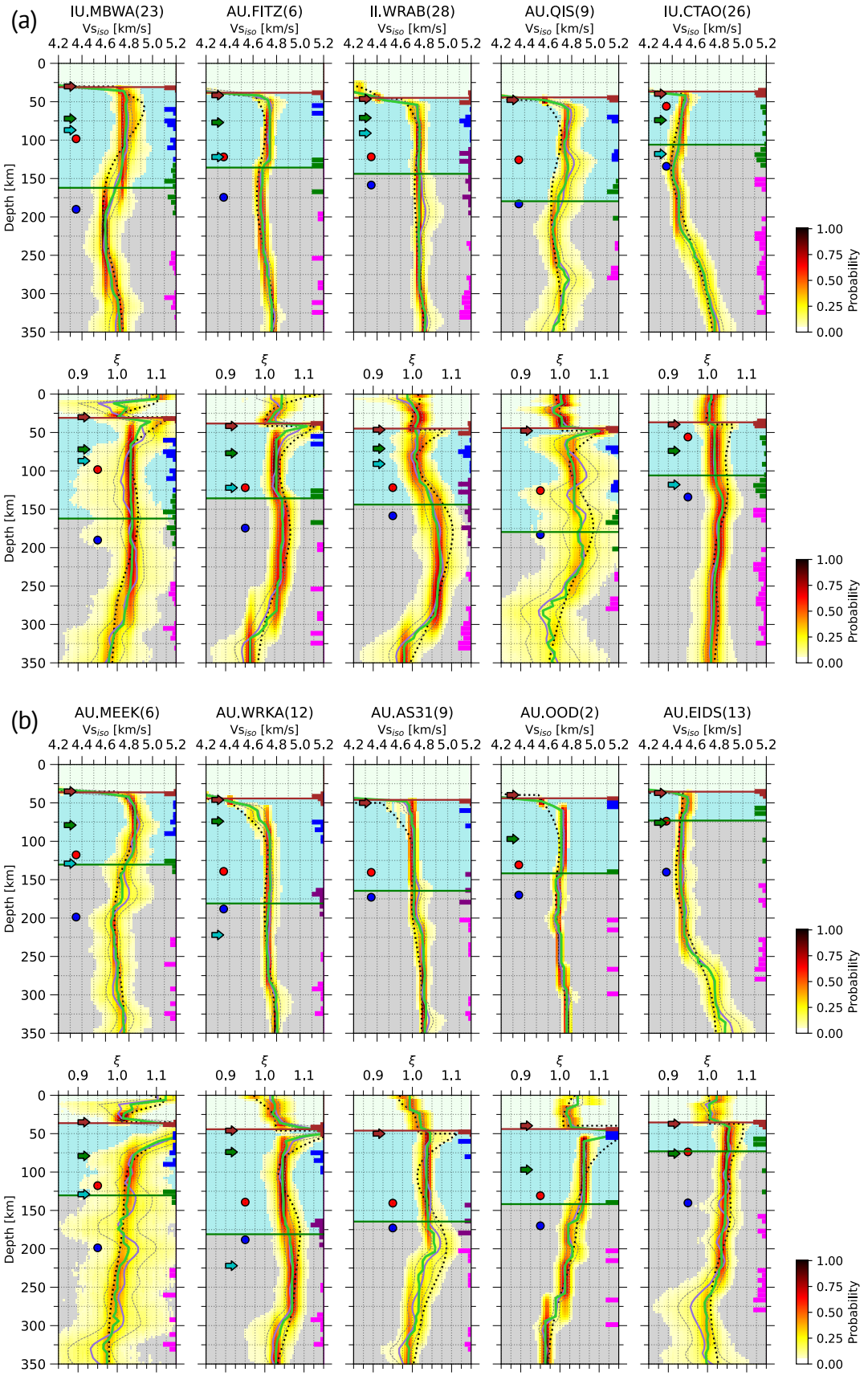
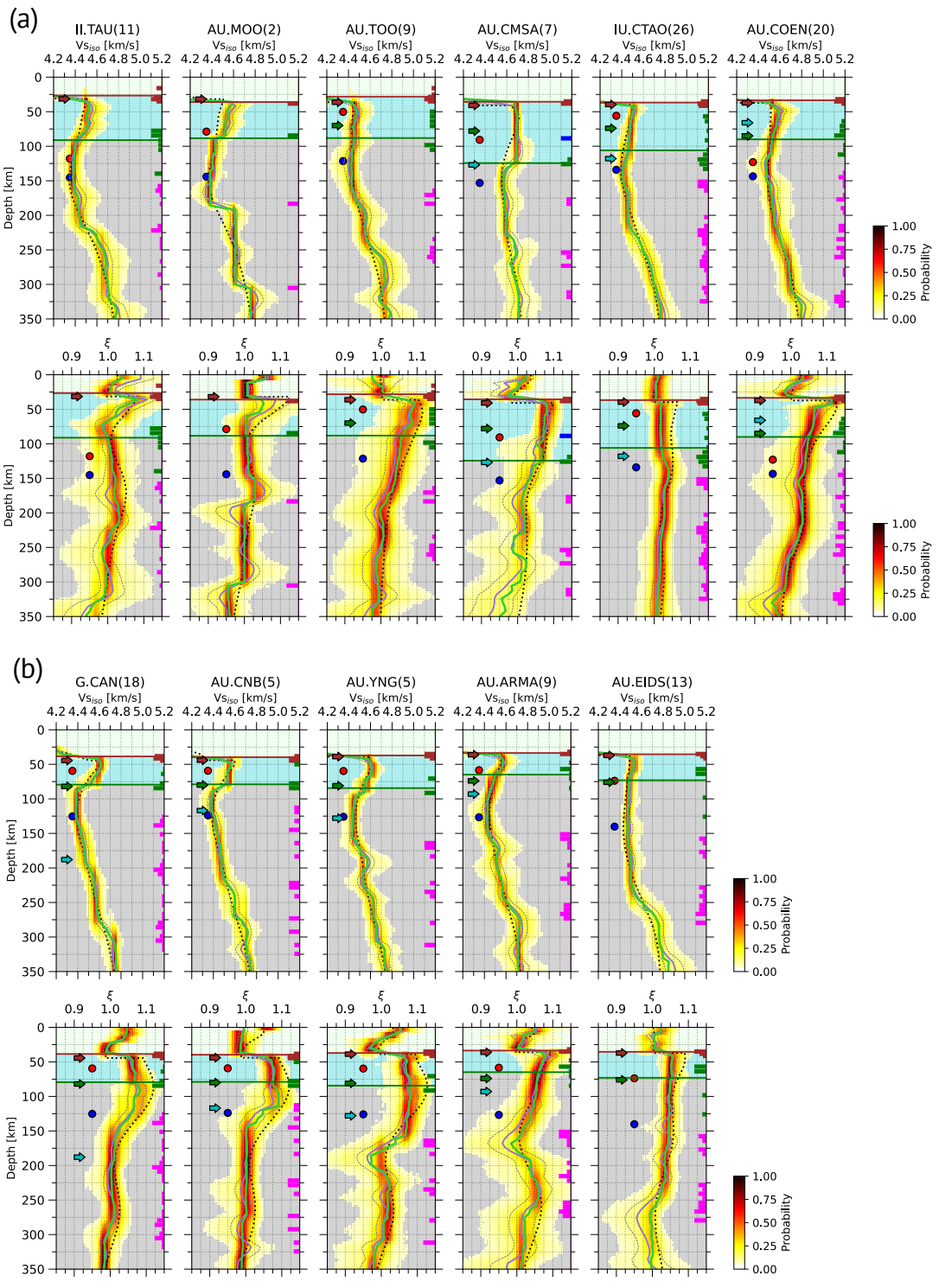

(a)
IU.MBWA(23)
AU.FITZ(6)
II.WRAB(28)
AU.QIS(9)
IU.CTAO(26)
Vs$_{iso}$ [km/s]
4.2 4.4 4.6 4.8 5.0 5.2
ξ
0.9 1.0 1.1
Depth [km]
0 50 100 150 200 250 300 350
Probability
1.00 0.75 0.50 0.25 0.00
(b)
AU.MEEK(6)
AU.WRKA(12)
AU.AS31(9)
AU.OOD(2)
AU.EIDS(13)

Figure S6: Same as Figures 4 and 5, but along (a) S20° and (b) S26°.



40

Figure S7: Same as Figures 4 & 5, but along (a) E145° and (b) S150°.

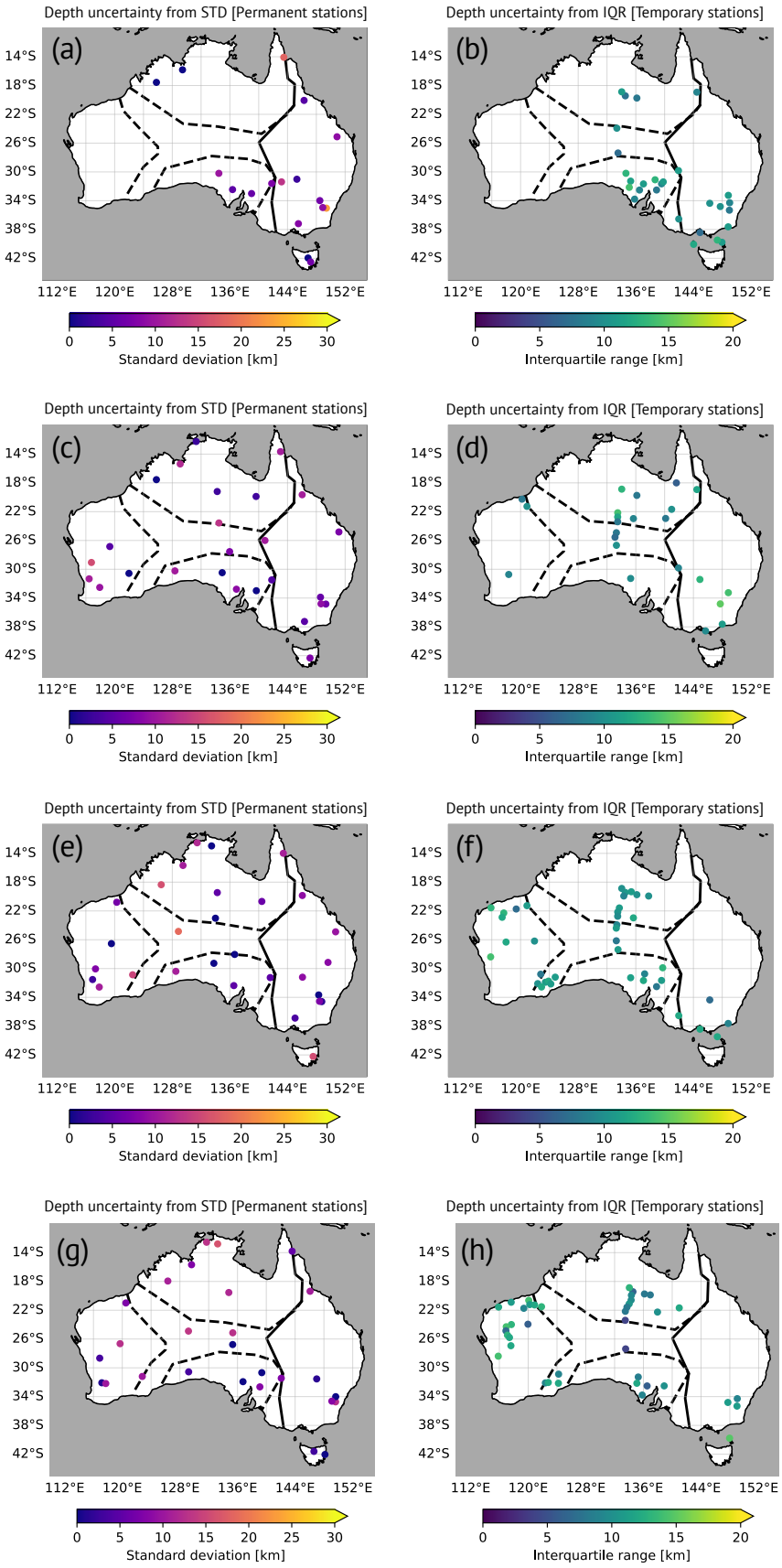

Depth uncertainty from STD [Permanent stations]
(a)
Depth uncertainty from IQR [Temporary stations]
(b)
Depth uncertainty from STD [Permanent stations]
(c)
Depth uncertainty from IQR [Temporary stations]
(d)
Depth uncertainty from STD [Permanent stations]
(e)
Depth uncertainty from IQR [Temporary stations]
(f)
Depth uncertainty from STD [Permanent stations]
(g)
Depth uncertainty from IQR [Temporary stations]
(h)
14°S
18°S
22°S
26°S
30°S
34°S
38°S
42°S
112°E
120°E
128°E
136°E
144°E
152°E
0
5
10
15
20
25
30
Standard deviation [km]
Interquartile range [km]

Figure S8: Uncertainties of the four clustered X-Ds (a,b: 170km-D, c,d: 220km-D, e,f: 270km-D, g,h: 310km-D). (a, c, e, g) Standard deviations of each of the X-D depths beneath the permanent stations, derived from the azimuth-dependent conversion points. (b, d, f, h) Interquartile ranges (IQRs) of X-D depths beneath temporary stations.

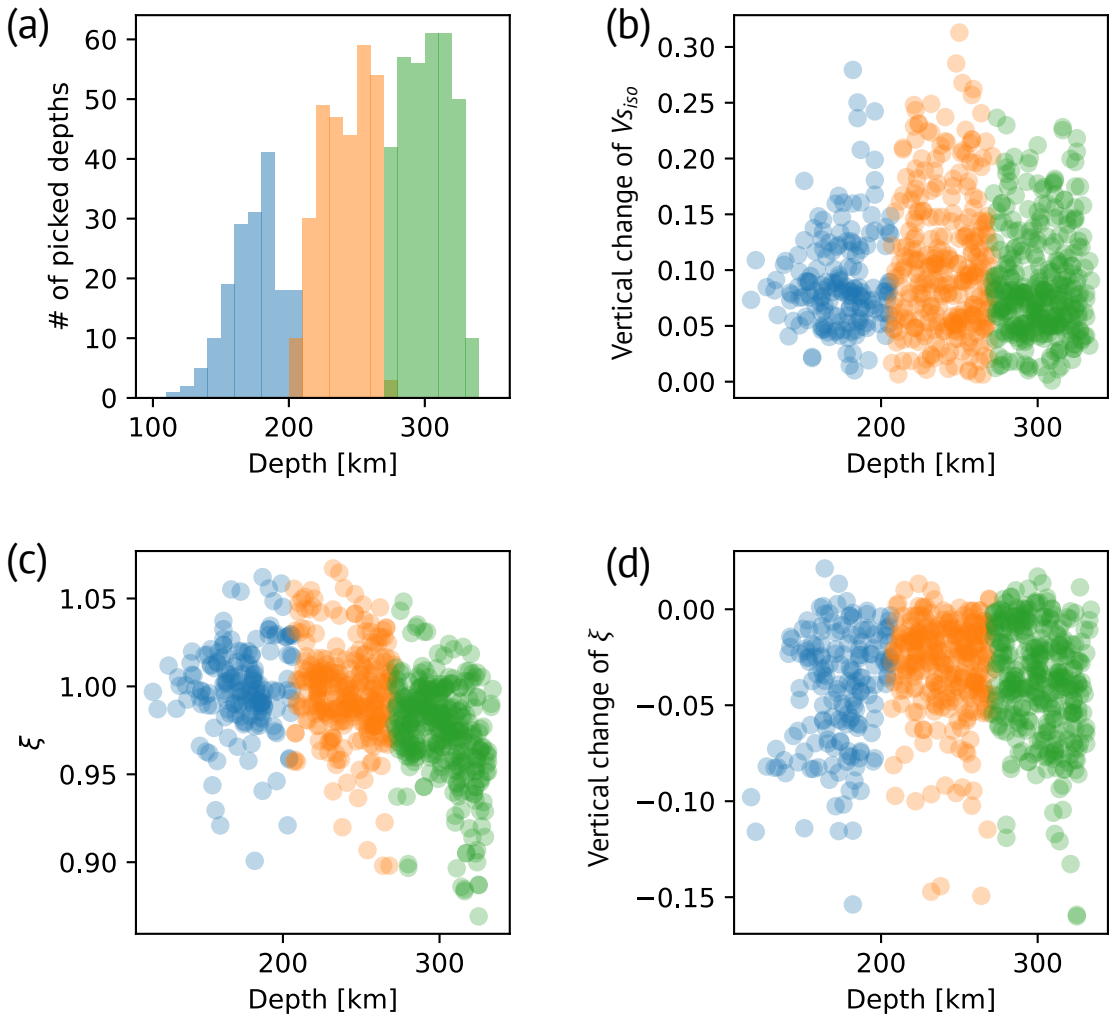


Figure S9: Same as Figure 10, but for $N_c = 3$ case. Color notations are identical to those in Figure 10, except that the 4th cluster is excluded here. In this case, the X-Ds are identified at three distinct depths: around 170 km, 260 km, and 310 km.

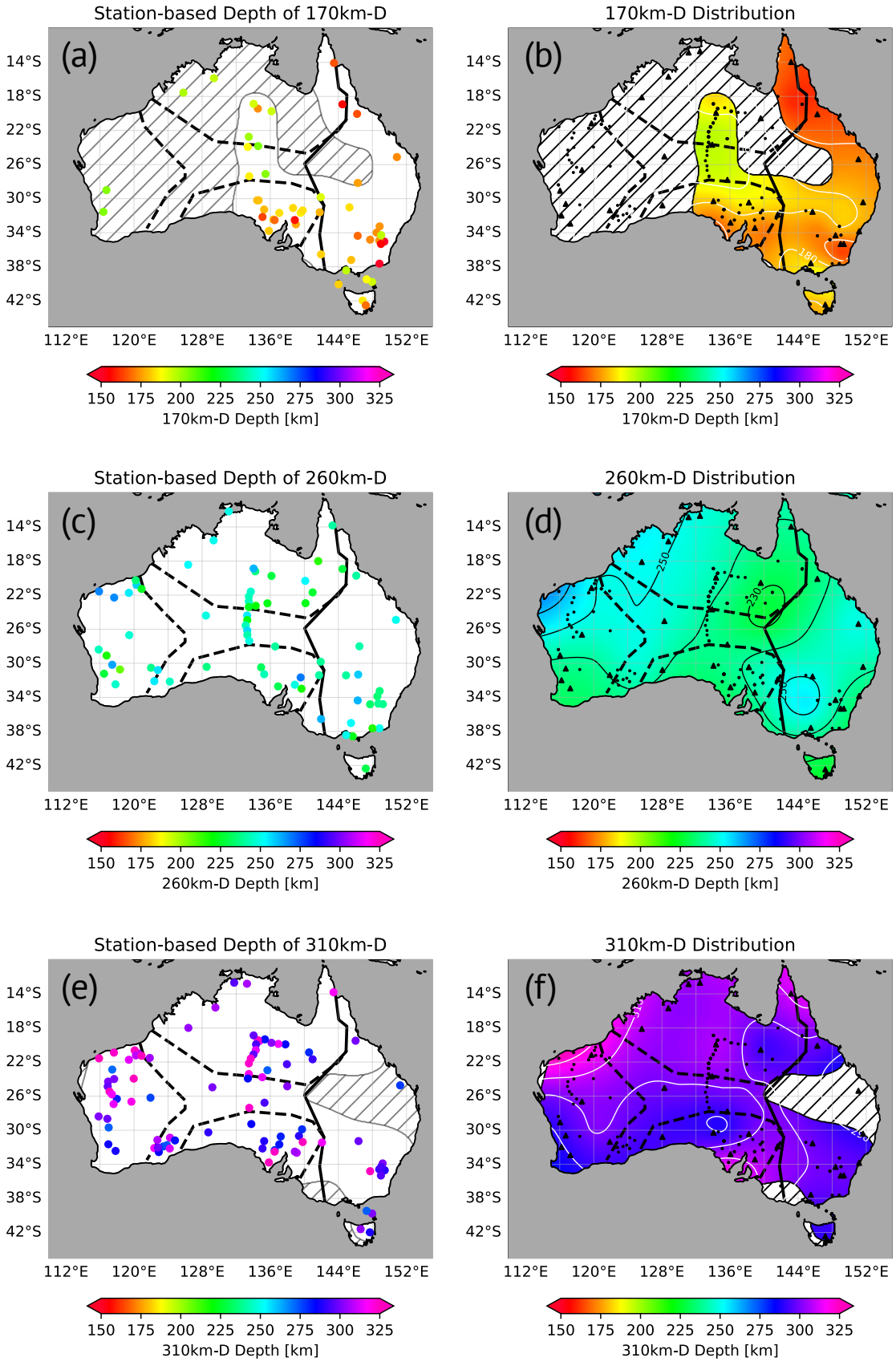

Station-based Depth of 170km-D
(a)
170km-D Distribution
(b)
Station-based Depth of 260km-D
(c)
260km-D Distribution
(d)
Station-based Depth of 310km-D
(e)
310km-D Distribution
(f)
14°S
18°S
22°S
26°S
30°S
34°S
38°S
42°S
112°E
120°E
128°E
136°E
144°E
152°E
150 175 200 225 250 275 300 325
170km-D Depth [km]
260km-D Depth [km]
310km-D Depth [km]

Figure S10: Same as Figure 11, but for the $N_c = 3$ case.

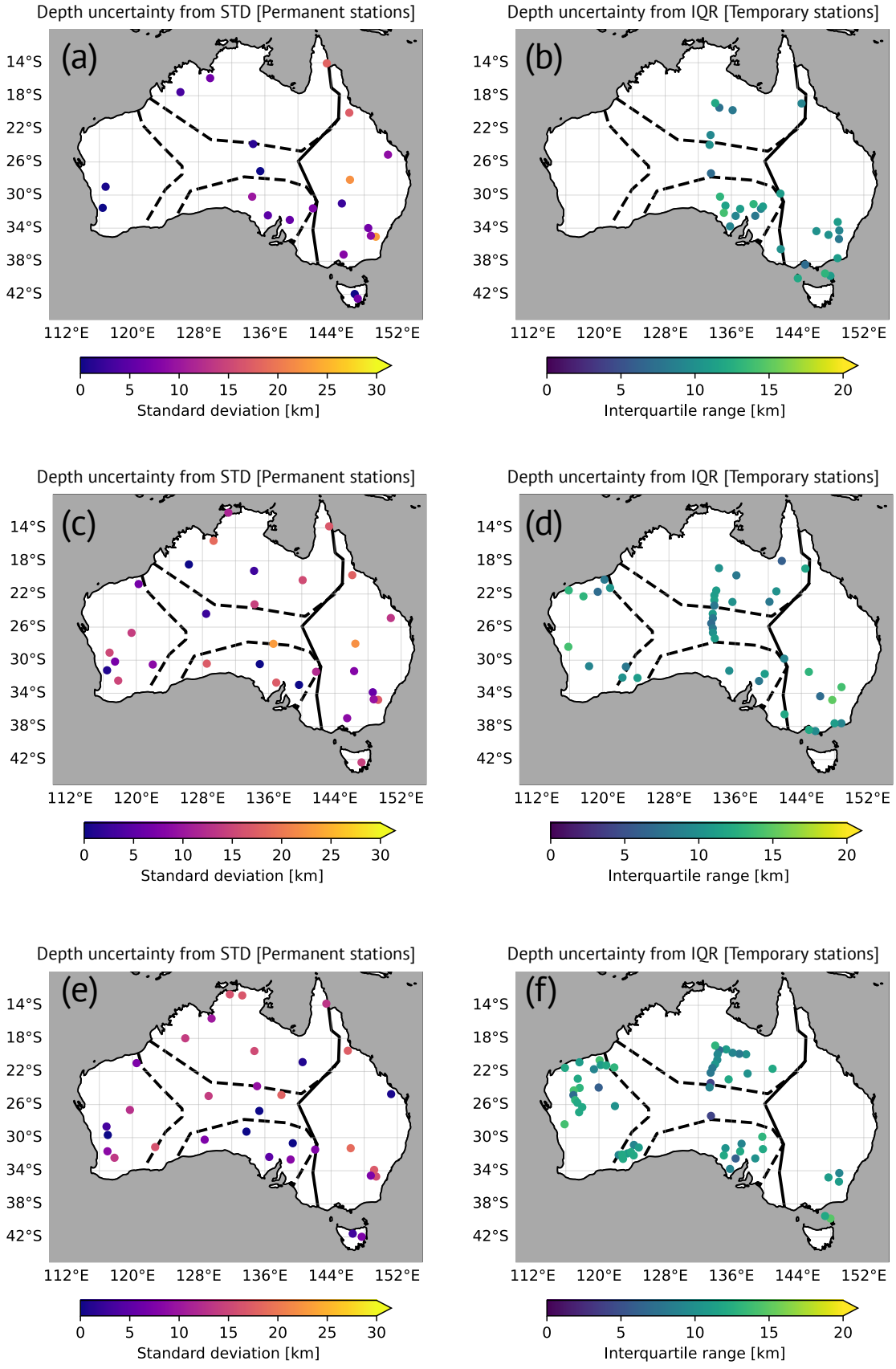

Depth uncertainty from STD [Permanent stations]
(a)
14°S
18°S
22°S
26°S
30°S
34°S
38°S
42°S
112°E
120°E
128°E
136°E
144°E
152°E
0
5
10
15
20
25
30
Standard deviation [km]
Depth uncertainty from IQR [Temporary stations]
(b)
0
5
10
15
20
Interquartile range [km]
Depth uncertainty from STD [Permanent stations]
(c)
Standard deviation [km]
Depth uncertainty from IQR [Temporary stations]
(d)
Interquartile range [km]
Depth uncertainty from STD [Permanent stations]
(e)
Standard deviation [km]
Depth uncertainty from IQR [Temporary stations]
(f)
Interquartile range [km]

Figure S11: Same as Figure S8, but for the $N_c = 3$ case.

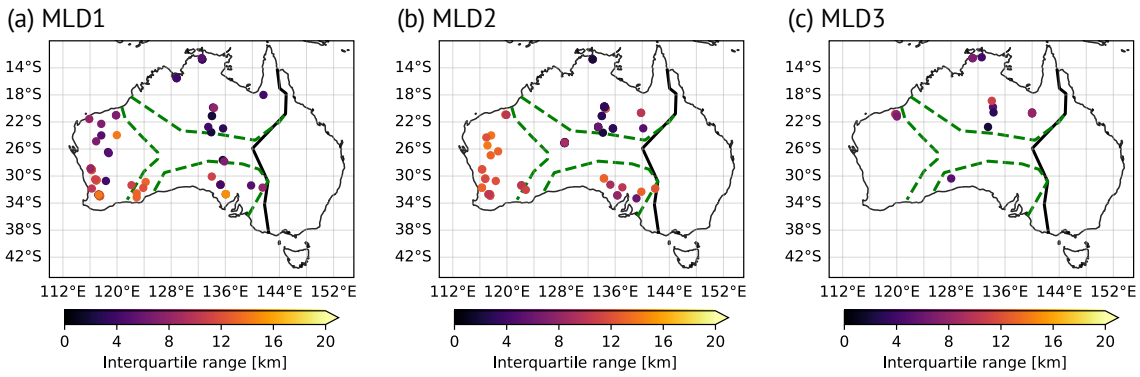


Figure S12: Interquartile range of MLD depths: (a) MLD1, (b) MLD2, (c) MLD3.

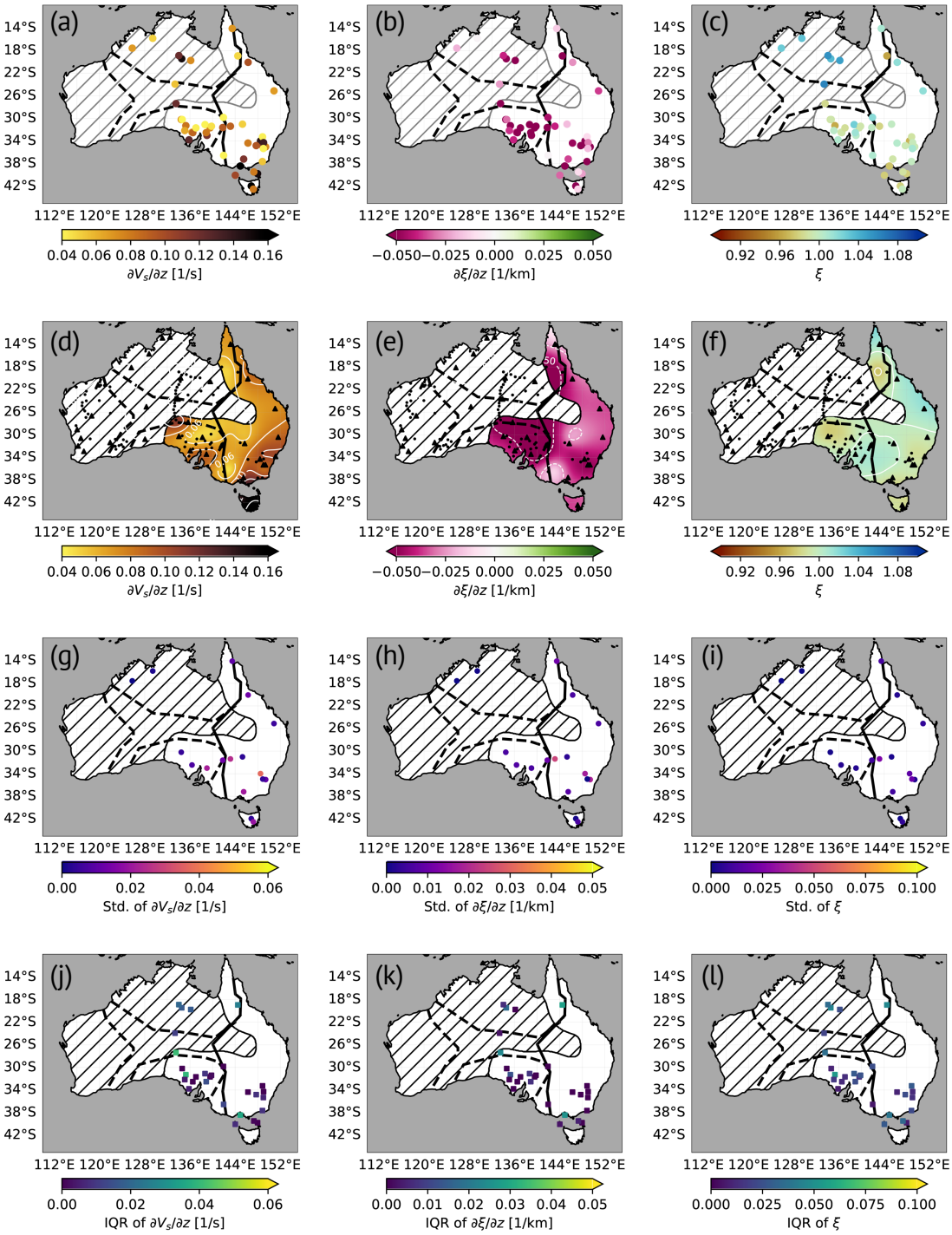


Figure S13: Mapping results of elastic properties for the 170km-D of four clustered X-Ds. (a-c) Station-based vertical (downward) changes in (a) isotropic S-wave velocity and (b) radial anisotropy across the 170km-D, and (c) absolute radial anisotropy below the 170km-

D. (d-f) Same as (a–c), but shown as spatially interpolated contour maps. (g-i) Uncertainties for permanent stations, represented by standard deviations derived from azimuth-dependent conversion points. (j-l) Same as (g-i), but for temporary stations, showing interquartile ranges estimated from the posterior distributions.

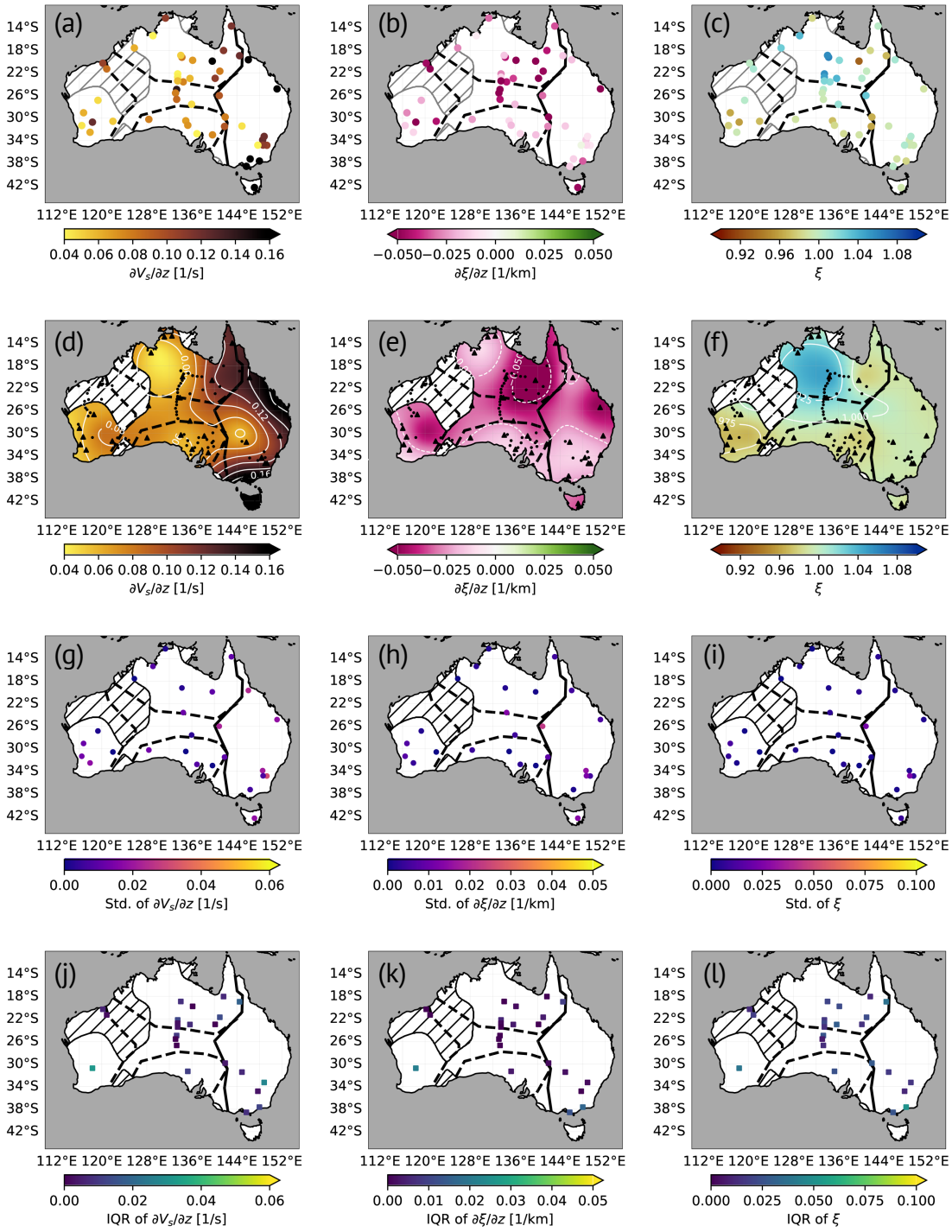


Figure S14: Same as Figure S13, but for the 220km-D.

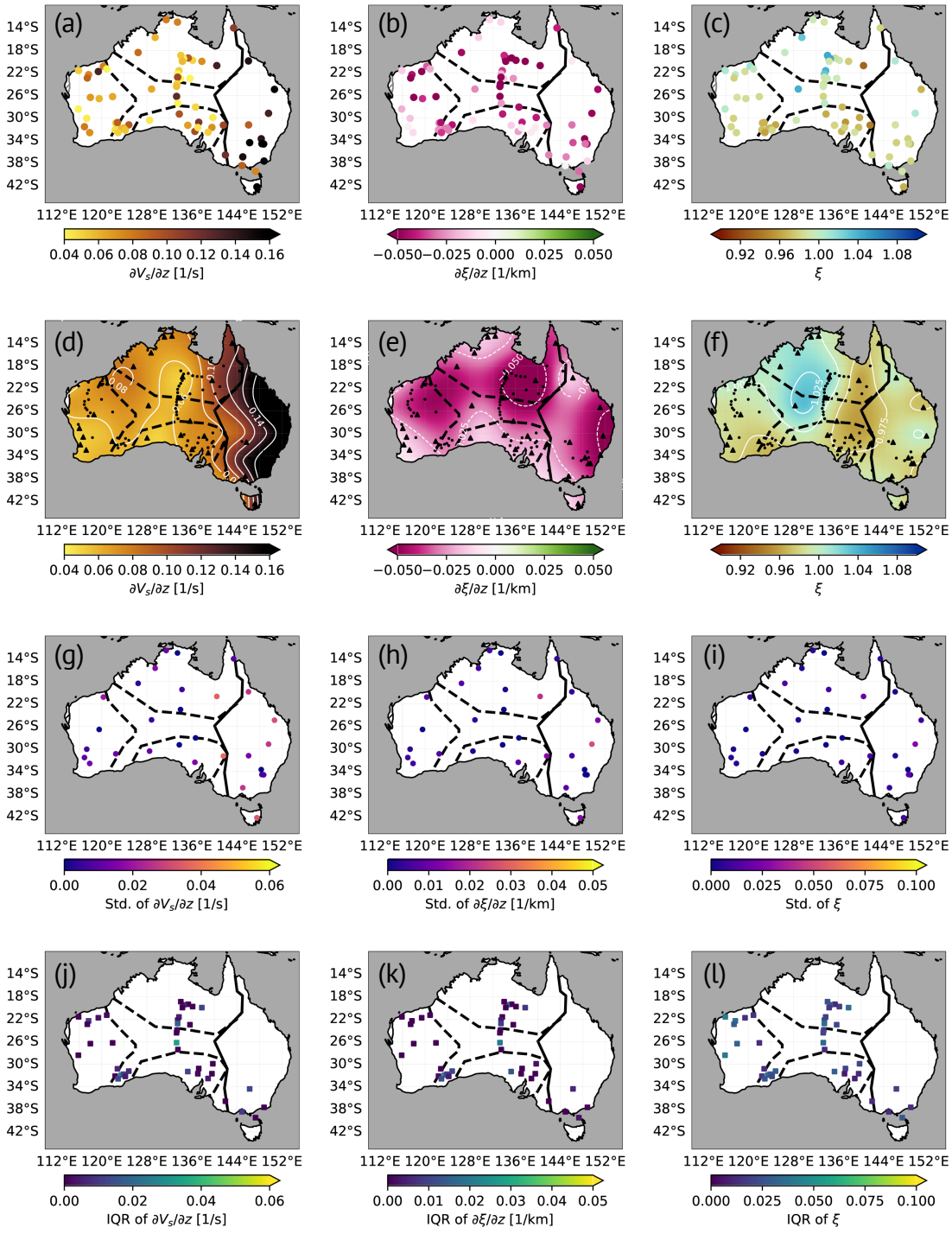


Figure S15: Same as Figure S13, but for the 270km-D.

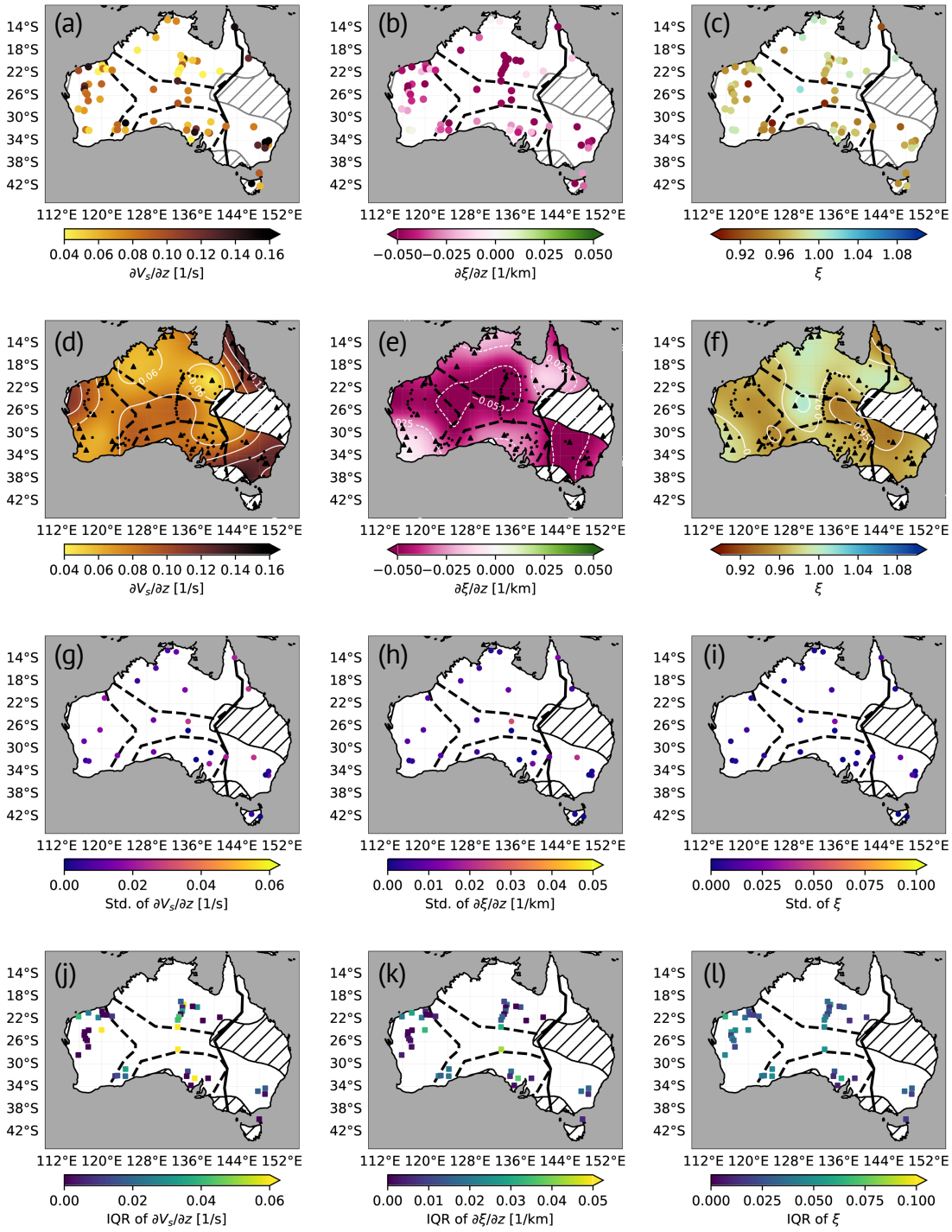


Figure S16: Same as Figure S13, but for the 310km-D.

Tkalčić, H., Chen, Y., Liu, R., Zhibin, H., Sun, L., Chan, W., 2011. Multistep modelling of teleseismic receiver functions combined with constraints from seismic tomography: crustal structure beneath southeast China. Geophys J Int 187, 303–326. https://doi.org/10.1111/j.1365-246x.2011.05132.x

Yoshizawa, K., 2014. Radially anisotropic 3-D shear wave structure of the Australian lithosphere and asthenosphere from multi-mode surface waves. Phys Earth Planet In 235, 33–48. https://doi.org/10.1016/j.pepi.2014.07.008